nature communications

Article

https://doi.org/10.1038/s41467-025-62255-2

Identification of Neuritin 1 as a local metabolic regulator of brown adipose tissue

Received: 20 March 2024

Accepted: 7 July 2025

Published online: 04 September 2025

Check for updates

Manuela Sánchez-Feutrie[1,2,3,4] ✉, Montserrat Romero[1,2,4,5], Sónia R. Veiga[1,2,4], Núria Borràs-Ferré[1,2,4,5], Nick Berrow[1], Martina Ràfols[1], Noemí Giménez[1], Andrea Rodgers-Furones[1,11], Alba Sabaté-Pérez[1,2,4,12], Ángela Rodríguez Pérez[1], Luis Rodrigo Cataldo[1,13,14], Hans Burghardt[1,2,4], David Sebastián[1,4,15], Natàlia Plana[1], Vanessa Hernández[1], Laura Isabel Alcaide[1], Óscar Reina[1], Maria J. Monte[6], José Juan G. Marin[6], Manuel Palacín[1,2,7], Remy Burcelin[8], Per Antonson[9], Jan-Ake Gustafsson[9,10] & Antonio Zorzano[1,2,4] ✉

Brown adipose tissue (BAT) plays a key role in metabolic homeostasis through its thermogenic effects and the secretion of regulatory molecules. Here we report that RAP250 haploinsufficiency stimulates BAT in mice, thus contributing to a decrease in fat accumulation. Local in vivo AAV-mediated RAP250 silencing in BAT reduces body weight and fat mass and enhances glucose oxidation, thereby indicating that RAP250 participates in the regulation of BAT metabolic activity. Analysis of the mechanisms led to the finding that Neuritin 1 is produced and released by brown adipocytes, it plays a key metabolic role, and it participates in the enhanced BAT metabolic activity under RAP250 deficiency. Forced overexpression of Neuritin 1 in UCP1-expressing cells markedly decreases fat mass and body weight gain in mice and induces the expression of thermogenic genes in BAT. Neuritin 1-deficient brown adipocytes also shows a reduced β-adrenergic response. We demonstrate a metabolic role of BAT-derived Neuritin 1 acting through an autocrine/paracrine mechanism. Based on our results, Neuritin-1 emerges as a potential target for the treatment of metabolic disorders.

Obesity has reached epidemic proportions, affecting 650 million people worldwide (https://www.who.int/news-room/fact-sheets/detail/obesity-and-overweight). Comorbidities of obesity—most notably type 2 diabetes mellitus (T2D), atherosclerosis, hypertension, and hyperlipidemia—are now major public health concerns[1]. Recent data also indicate that obesity is associated with a more severe clinical course of COVID-19 and risk of fatality[2,3]. Thus, there is an urgent need to delineate the precise mechanisms that underlie the onset of obesity and metabolic syndrome.

Brown adipose tissue (BAT) is an organ specialized in performing non-shivering thermogenesis, and it is present in adult human subjects[4–6]. The capacity of thermogenic fat to oxidize substrates and increase energy expenditure has drawn growing interest as a therapeutic approach to tackle obesity and associated metabolic disorders[7]. BAT thermogenesis requires the release of norepinephrine from local sympathetic axons; norepinephrine activates the β-adrenergic receptor-cAMP-PKA pathway in brown adipocytes to drive lipolysis and thermogenic respiration[8]. The release of norepinephrine from sympathetic nerves and β3-adrenergic receptor binding to brown adipocytes determine the level of thermogenesis in BAT by regulating the activity of lipases, providing the immediate fuel molecules for BAT mitochondria and heat production[8]. Recent data indicate that brown adipocytes secrete multiple signaling molecules, named batokines, including FGF21, Myostatin, CXCL14, EPDR1 and

A full list of affiliations appears at the end of the paper. ✉e-mail: manuela.sanchez@irbbarcelona.org; antonio.zorzano@irbbarcelona.org

adiponectin, among others, which operate as endocrine factors[9–14]. Other batokines work as local autocrine/paracrine factors, as reported for BMP7, BMP8b, NRG4, and S100b[15–18]. Regarding the locally-acting factors, some of them are produced by vascular cells, while others are generated by brown adipocytes[15–18]. The action of these local factors is highly variable, ranging from effects promoting neurite outgrowth from sympathetic neurons to direct effects on the metabolism of brown adipocytes.

RAP250 (encoded by *NCOA6* gene) is a co-activator of nuclear hormone receptors. It also transactivates other transcription factors such as c-Jun, c-Fos, ATF-2, CBP, heat shock factor 1, SRF, E2F-1, Rb, NFκβ, and C/EBPα[19]. RAP250 is also an integral and unique component of a Set1-like complex named ASCOM (for ASC-2 complex), which contains histone H3-Lys-4-methyltransferase (H3K4MT) MLL3 or its paralogue MLL4[20,21]. RAP250 is a pleiotropic modulator that affects growth, development, reproduction, apoptosis, and wound healing[22]. In addition, it participates in liver metabolism[23,24] and modulates insulin secretion in mice and humans[25,26], and it is required for white adipogenesis in vitro[27]. *MLL3*$^{\Delta/\Delta}$ mice show decreased adiposity and enhanced insulin sensitivity, although the underlying target tissues were not studied[28].

In this work, we focused on the metabolic effects caused by the haploinsufficiency of RAP250. We report that RAP250 modulates the thermogenic activity of BAT in mice. Surprisingly, BAT from RAP250-deficient mice showed enhanced expression of Neuritin 1 (Nrn1), a protein that impacts on the central nervous system[29–32]. AAV-mediated expression of Nrn1 in brown adipose cells caused metabolic effects leading to a reduction in fat mass and the induction of BAT thermogenic genes. The repression of Nrn1 in brown adipose cells disrupted the capacity of these cells to respond to a β-adrenergic receptor agonist.

Results

Heterozygous RAP250 knockout mice show a lean phenotype, resistance to diet-induced obesity, and enhanced insulin sensitivity

Based on previous reports indicating that RAP250 regulates metabolic homeostasis[23–28], we examined whether it plays a relevant role in energy metabolism. To this aim, we monitored the phenotype of male mice heterozygous for RAP250 (RAP250$^{+/}$) since homozygous knockout mice show prenatal lethality[33]. Heterozygous mice showed an almost 50% decrease in RAP250 expression in inguinal (ING) adipose tissue, brown (BAT) adipose tissue and skeletal muscle (Fig. S1A–F). Control (wild-type, WT) and RAP250$^{+/-}$ male mice showed a similar body weight at 10 weeks of age but later diverged, the latter being leaner, despite increased food intake (Fig. 1A, B). Thirty-week-old male RAP250$^{+/-}$ mice also showed smaller inguinal (ING) and perigonadal (PAT) adipose tissues compared with control animals (Fig. 1C, D). However, no differences in heart, skeletal muscle or liver weight were detected (Fig. S1G). We monitored the gain of adipose tissue volume by microCT in several sets of male mice. Data revealed that the differences in the size of subcutaneous and visceral depots (the latter defined as the sum of omental, mesenteric, retroperitoneal and perigonadal depots) were fully established at 30 weeks of age and were maintained thereafter (Fig. 1E–G). In keeping with a reduced adipose mass, male RAP250$^{+/-}$ mice showed a markedly reduced adipose cell size (Fig. 1H, I) and low plasma leptin levels (Fig. 1J). Total DNA present in ING or PAT adipose tissues was similar in control and RAP250$^{+/-}$ male mice (Fig. 1K), thereby suggesting no changes in cellularity. Thirty-seven-week-old but not thirty-week-old female RAP250$^{+/-}$ mice showed a reduced body weight compared to controls (Fig. S1H). ING or PAT adipose depots were also reduced in female RAP250$^{+/-}$ mice at the age of 37 weeks (Fig. S1I). Total DNA present in ING or PAT adipose tissues was similar in control and RAP250$^{+/-}$ female mice (Fig. S1J).

Next, we analyzed the response of RAP250$^{+/-}$ mice to a high-fat diet (HFD). Male mice subjected to a 60% fat diet gained body weight throughout the experiment (Fig. S2A), and RAP250$^{+/-}$ mice consistently remained leaner than control counterparts (Fig. S2A) under conditions in which food intake was similar in both genotypes (Fig. S2B). HFD-treated RAP250$^{+/-}$ mice also showed a smaller visceral fat depot (Fig. S2C) and lower plasma leptin levels compared to control animals (Fig. S2D). Female RAP250$^{+/-}$ mice also showed a lower body weight and reduced adipose depots after a HFD (Fig. S2E and F). These data reveal that male and female RAP250$^{+/-}$ mice are resistant to HFD-induced obesity.

Upon fasting, male RAP250$^{+/-}$ mice showed normal levels of plasma glucose, adiponectin and free fatty acids, and reduced concentrations of plasma insulin, triglycerides and cholesterol on a normal diet (ND) (Fig. 2A, B, and Table S1). Administration of a HFD for 20 weeks caused high plasma concentrations of glucose and insulin in control male mice, but concentrations remained within the normal range in RAP250$^{+/-}$ counterparts (Fig. 2C, D). Studies performed in 30-week-old male RAP250$^{+/-}$ mice on a standard diet showed improved glucose tolerance and enhanced insulin secretion compared to control mice (Fig. 2E and F). Glucose tolerance was also improved in male RAP250$^{+/-}$ mice fed with HFD (Fig. 2G), and under these conditions, plasma insulin was markedly attenuated (Fig. 2H).

Female RAP250$^{+/-}$ mice showed no changes in plasma glucose or insulin under a standard diet or HFD (Fig. S3A, B). Thirty-week-old female RAP250$^{+/-}$ mice subjected to either a standard diet or HFD also showed enhanced glucose tolerance in the absence of changes in plasma insulin levels (Fig. S3C–F).

The impact of RAP250 deficiency on whole-body glucose utilization was also monitored in conscious male mice on a normal diet during a euglycemic-hyperinsulinemic clamp (Fig. 2I). Under hyperinsulinemia, RAP250$^{+/-}$ mice showed an increase in whole-body glucose infusion rate (GIR), glucose turnover (Turnover), whole-body glycolysis, and glycogen synthesis rate (Fig. 2I). Thus, these animals were indeed more insulin-sensitive than control mice. Moreover, hepatic steatosis induced by the HFD was prevented in RAP250$^{+/-}$ male mice, as reflected by large differences in hepatic fat deposition (Fig. 2J and K). In all, this pattern of changes suggests that RAP250$^{+/-}$ mice of both sexes show improved glucose tolerance as a consequence of the improved insulin sensitivity, which occurs even in the absence of changes in adiposity.

RAP250 deficiency enhances energy expenditure and the metabolic activity of brown adipose tissue

We next questioned whether the reduced adiposity detected in RAP250$^{+/-}$ mice derives from a higher rate of energy expenditure, thereby explaining a lower fat content and a parallel increased food intake. Indeed, RAP250$^{+/-}$ mice showed improved whole-body O_2 consumption and CO_2 production, as shown by ANCOVA analysis (Fig. 3A and S4A). Energy expenditure, glucose oxidation, and the respiratory exchange ratio (RER) were also increased (Fig. 3B, C, S4B and C). This enhancement occurred in the absence of alterations in ambulation (Fig. S4D). Exposure of control and RAP250$^{+/-}$ mice to a HFD for 20 weeks maintained most of the alterations detected under a standard diet, such as increased O_2 consumption, CO_2 production, energy expenditure, and lipid oxidation (Fig. S4E–H), and again, no changes in locomotor activity were detected (Fig. S4I).

Given these observations, we explored the involvement of BAT in this phenotype. Interscapular BAT mass was reduced in RAP250$^{+/-}$ mice (Fig. 3D), and glucose oxidation was markedly enhanced in isolated brown adipocytes obtained from RAP250$^{+/-}$ mice (Fig. 3E). In addition, histological examination revealed less accumulation of lipids and a smaller lipid droplet size in RAP250-deficient brown adipocytes (Fig. 3F and G). Additional histological analyses using wheat germ agglutinin (WGA, to label the cell surface), DAPI (to label the nuclei),

https://doi.org/10.1038/s41467-025-62255-2

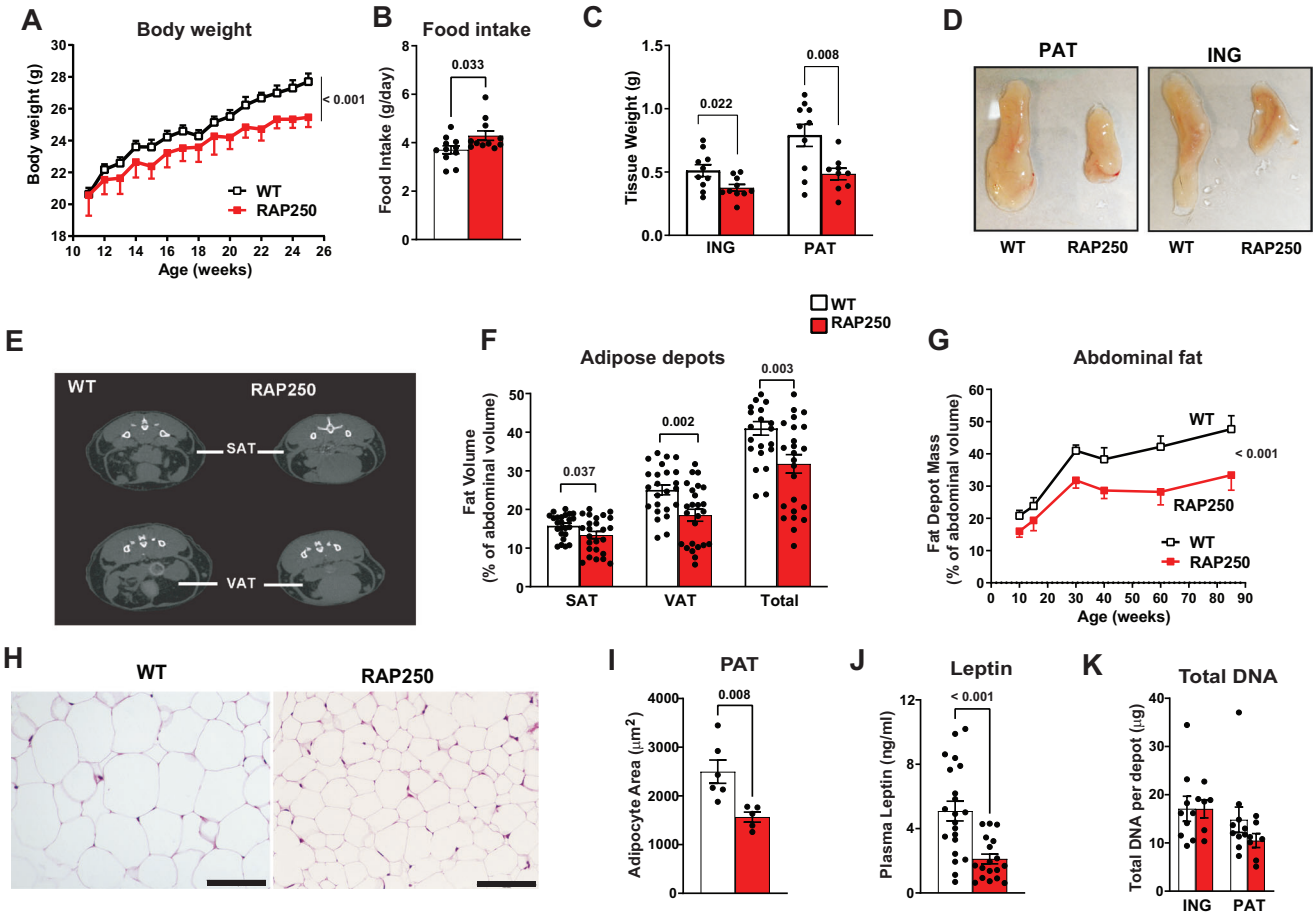

Fig. 1 | RAP250$^{+/-}$ mice show a lean phenotype. A Body weight curves for 12- to 25-week-old male mice. Data are expressed as grams of body weight (WT n = 6, black open symbols; RAP250$^{+/-}$ n = 5, red symbols, and labeled as RAP250). **B** Food intake as grams of daily intake in 20- to 30-week-old mice (n = 11). **C** Inguinal adipose tissue (ING) and Perigonadal adipose tissue (PAT). Data are expressed as grams of tissue weight (n = 10). **D** Representative images of PAT and ING depots from WT and RAP250$^{+/-}$ male mice. **E** Transversal gray scale image of mouse abdominal region showing the subcutaneous adipose mass (SAT) and visceral adipose mass (VAT); vertebrae are seen as the denser white structures; least dense areas represent the adipose mass, and the layer that separates the visceral compartment from the subcutaneous region can be observed. **F** MicroCT adipose volume estimation of SAT, VAT and total abdominal adipose volume (n = 24) of 30-week-old male mice. Data are expressed as percentage of fat volume (femoral head to L5 vertebra). **G** Progression of total abdominal fat volume in time, measured by microCT Scan, in the same cohort of mice (10 weeks n = 8; 15 weeks n = 7; 30 weeks WT n = 24 and RAP250$^{+/-}$ n = 25; 40 weeks n = 10; 60 weeks n = 16 for WT and n = 11 for RAP250$^{+/-}$; 85 weeks n = 8 for WT and n = 6 for RAP250$^{+/-}$). **H** PAT paraffin slices stained with Hematoxylin/Eosin (scale bar=100 μm). **I** PAT adipocyte cell size of 30-week-old male mice (n = 5, 52–200 cells counted per animal). **J** Plasma leptin in 16-h fasted 30-week-old male mice (n = 22 for WT, n = 18 for RAP250$^{+/}$). **K** Total DNA in ING and PAT depots of male mice. Data are expressed as μg of DNA per depot (in ING depots n = 9 for WT and n = 6 for RAP250$^{+/-}$, in PAT depots n = 10 for WT and n = 7 for RAP250$^{+/-}$). Data are MEAN+/− SEM. Statistical differences according to a two-sided Student´s *t* test (**B**, **C**, **F**, **I**, **J** and **K**) and Ordinary two-way ANOVA (**A** and **G**). Source data are provided as a Source Data file.

and anti-UCP1 antibody (to measure the differentiation state of adipocytes) were performed in BAT sections. Triple staining showed an increased abundance of UCP1 in brown adipocytes from RAP250$^{+/-}$ mice, consistent with an enhanced metabolic activity (Fig. 3H and J). In addition, data showed a reduced adipose cell size in BAT from RAP250$^{+/-}$ mice (Fig. 3H and I). In contrast, no differences in adipose cell size were detected in ING fat (Fig. S4J and K). Electron microscopy also revealed the presence of larger mitochondria in brown adipose cells in these mice (Fig. S4L and M).

To further study the alterations in BAT caused by RAP250 deficiency, we performed RNA-Seq analysis. More than 500 genes were significantly upregulated and more than 330 were downregulated in BAT from RAP250$^{+/-}$ mice (Fig. 3K). In keeping with the RNA-seq analysis, the expression of adipogenic and thermogenic genes such as *Pparg2*, *Prdm16*, *Cebpa*, *Ppara*, *Dio2*, *Ppargc1a*, and *Ucp1* was markedly increased in RAP250-deficient BAT, as determined by real-time PCR assays (Fig. 3L). In addition, the abundance of proteins PPARγ, C/EBPα and UCP1 was increased in brown adipose tissue from RAP250$^{+/-}$ mice compared to controls (Fig. 3M and N). In all, these data highly support the view that BAT is metabolically more active in RAP250-deficient mice compared to control, and that it may contribute to enhanced energy expenditure in response to RAP250 deficiency.

Our data indicate that RAP250 is a negative regulator of BAT metabolism in mice. In order to further analyze this, we studied the impact of cold exposure on the BAT expression of RAP250. Exposure for 8 h to cold (4 °C) induced the expression of genes *Ucp1*, *Ppargca1*, and *Pde3b*, and this was accompanied by a marked repression of RAP250 gene expression (Fig. S5A). In parallel to these observations, exposure of brown adipocytes for 2 h in the presence of IBMX, a phosphodiesterase inhibitor induced Rgs2 and reduced RAP250 (Fig. S5B). This suggests that RAP250 participates in the activation of thermogenesis of brown adipocytes during cold and that the response is mediated by cAMP. In addition, RAP250 heterozygous mice showed a greater induction of Ucp1 mRNA levels in BAT in response to cold exposure (Fig. S5C). Under these conditions a greater induction of

https://doi.org/10.1038/s41467-025-62255-2

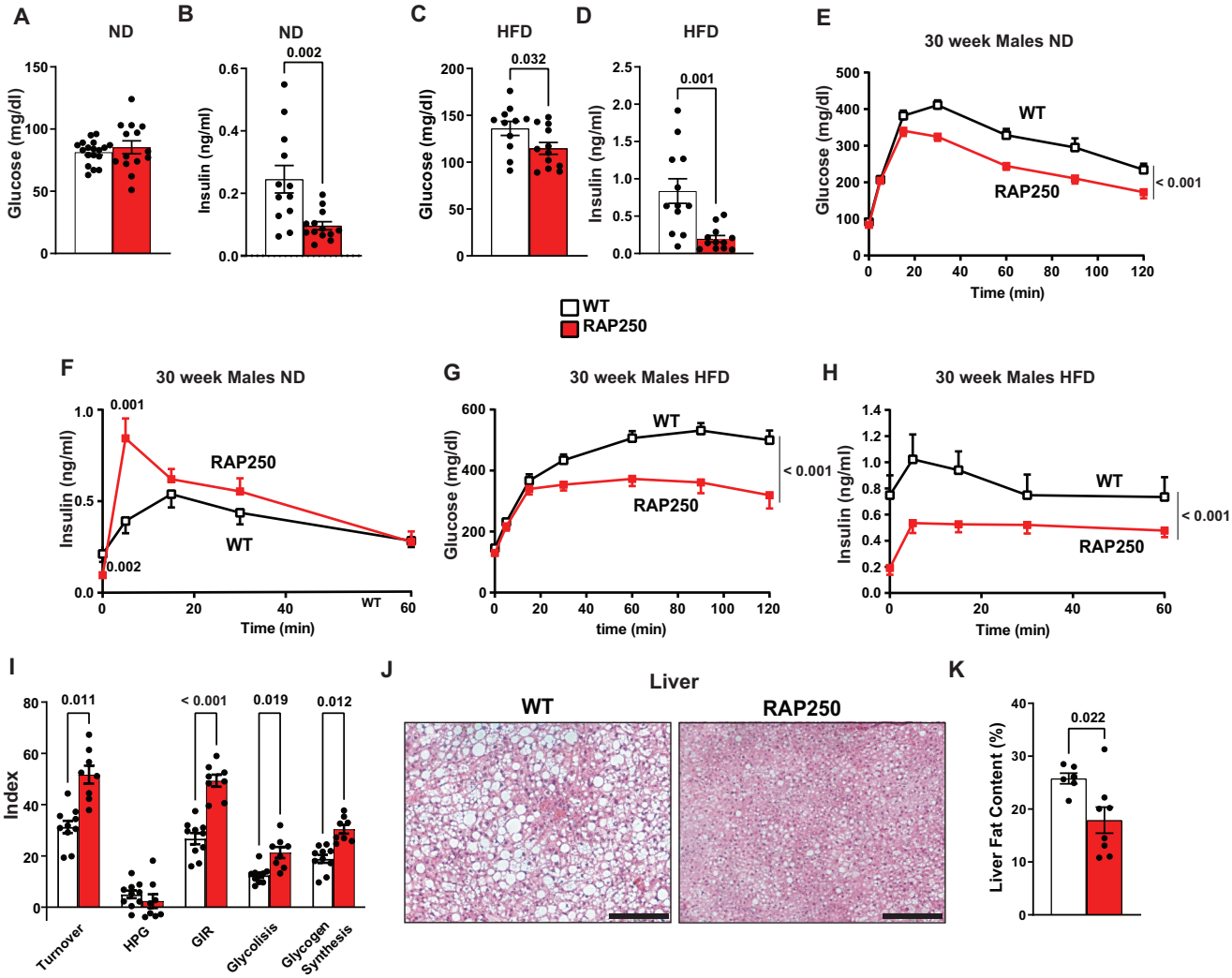

Fig. 2 | RAP250$^{+/-}$ mice show enhanced insulin sensitivity and are protected against insulin resistance induced by a high-fat diet. A Fasting plasma glucose (mg/dl) (WT n = 18 and RAP250$^{+/-}$ n = 14) and **B** insulin (ng/ml) levels (WT n = 14 and RAP250$^{+/-}$ n = 13) of 30-week-old male mice under a normal diet ND. **C** Fasting plasma glucose (n = 12) and **D** insulin levels (WT n = 10 and RAP250$^{+/-}$ n = 12) of 30-week-old male mice under a high-fat diet (HFD). **E** Plasma glucose (time 0 to 60 min WT n = 23 and RAP250$^{+/-}$ n = 22; time 90 and 120 WT n = 15 and RAP250$^{+/-}$ n = 14) and **F** insulin profiles (time 0 to 30 min WT n = 14 and RAP250$^{+/-}$ n = 13; time 60 WT n = 5 and RAP250$^{+/-}$ n = 5)) upon glucose tolerance test (2 mg/kg) in male mice on a normal diet. **G** Plasma glucose (WT n = 13 and RAP250$^{+/-}$ n = 12) and **H** insulin profiles (WT n = 13 and RAP250$^{+/-}$ n = 10) under glucose tolerance test (2 mg/kg) in male mice after 16 weeks on a HFD (n = 12). **I** Whole-body glucose turnover (Turnover), hepatic glucose production (HGP), whole-body glucose infusion rate (GIR), whole-body glycolysis rate (Glycolysis), and whole-body glycogen synthesis rate (Glycogen synthesis) were measured in a 3-h hyperinsulinemic-euglycemic clamp (1.5 mU/kg/min insulin) in 30-week-old male mice (n = 9 for WT and n = 8 for RAP250$^{+/-}$). **J** Hematoxylin/Eosin-stained paraffin slices of liver after 20 weeks of a HFD (scale bar=200 μm), and (**K**) Liver fat content as % of low density area (Lipid Droplets) over total histology slice area (n = 5, 25 slices per group). Data are MEAN+/− SEM. Statistical differences according to a two-sided Student´s *t* test (**B**, **C**, **D**, **F**, **I** and **K**) and Ordinary two-way ANOVA (**E**, **G**, and **H**). Source data are provided as a Source Data file.

glucose oxidation was also detected in RAP250$^{+/-}$ mice during cold (Fig. S5D).

Local repression of RAP250 in BAT phenocopies some of the metabolic alterations of RAP250$^{+/-}$ mice

Next, we addressed whether local alterations in BAT were sufficient to induce some of the metabolic alterations detected in RAP250$^{+/-}$ mice. To repress RAP250 in interscapular brown adipose, we injected adeno-associated viruses (AAVs) encoding shRNAs directed against RAP250, under H1 promoter, into the BAT of 2 month-old C57Bl/6 J mice (control mice were injected with AAVs encoding a scramble sequence). The injection of shRAP250 AAVs into this tissue reduced RAP250 expression (Fig. 4A and B), and this led to a significant decrease in body weight (Fig. 4C) and fat mass up to 10 weeks after the injection (Fig. 4D). In addition, shRAP250-injected mice showed enhanced glucose oxidation (Fig. 4E) and an improved respiratory exchange ratio (RER) (Fig. 4F). The expression of UCP1 protein was also enhanced in RAP250-deficient BAT (Fig. 4G). Under these conditions, plasma leptin levels remained unaltered (Fig. 4H).

In parallel studies, the perigonadal (epididymal) adipose tissue depots of 2 month-old C57Bl/6J male mice were injected with shRAP250- or scramble RNA-encoding AAVs. Data indicate that shRAP250 AAV administration reduced RAP250 expression in adipose tissue by 50% (Fig. S6A and B) 24 weeks after AAV injection. Under these conditions, body weight and total fat mass or perigonadal adipose depots were not altered in the RAP250-deficient group (Fig. S6C–E). RAP250 deficiency in WAT depots did not alter RER or glucose oxidation (Fig. S6F and G). Plasma leptin levels were not altered upon PAT gene manipulation (Fig. S6H). Based on our data, we propose that selective repression of RAP250 in BAT is the main driver

https://doi.org/10.1038/s41467-025-62255-2

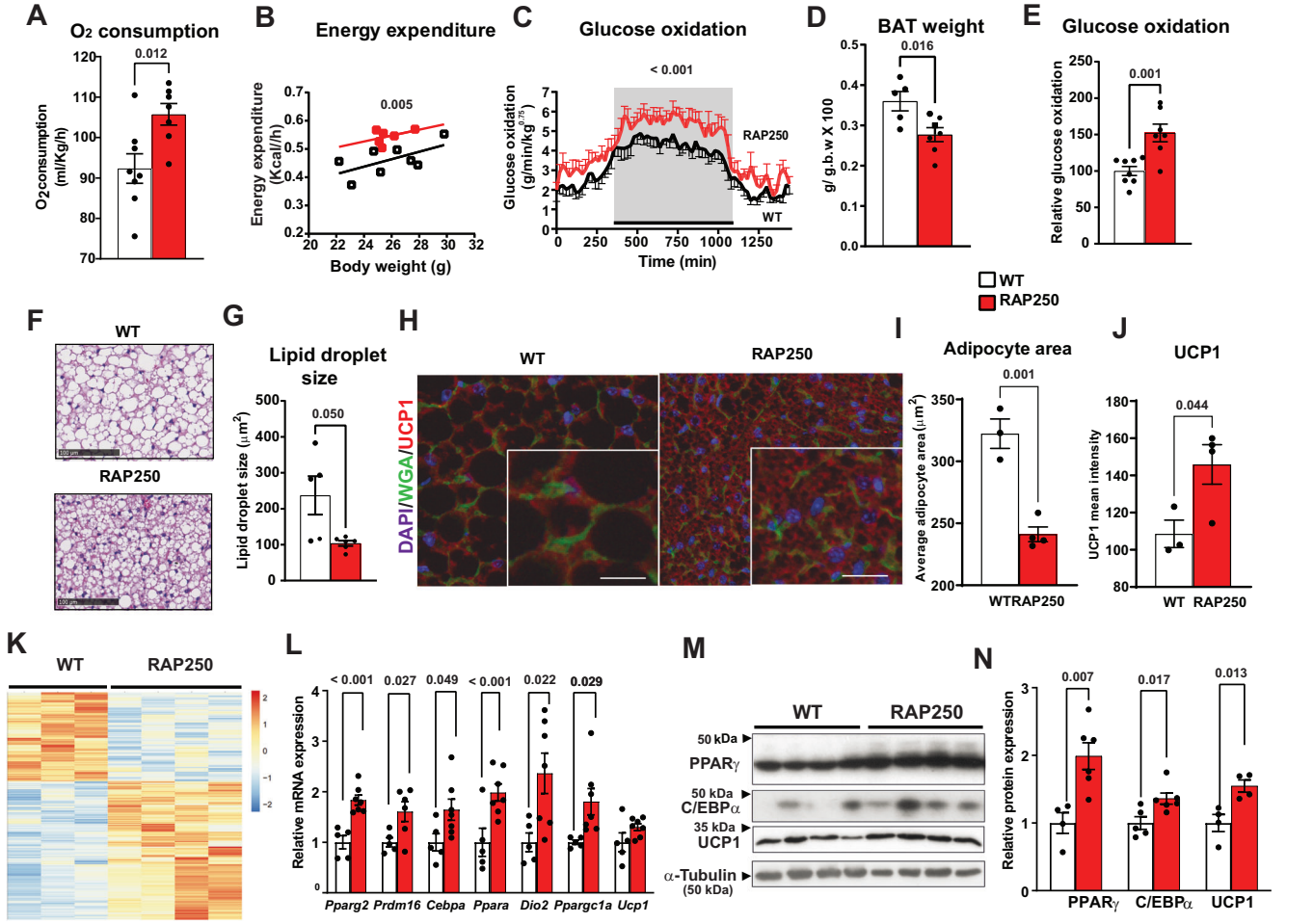

Fig. 3 | RAP250 deficiency enhances energy expenditure and BAT activity. **A** Whole-body oxygen consumption in male mice. Adjusted means based on a normalized mouse weight of 25.8071 g determined using ANCOVA (n = 8 for WT; n = 7 for RAP250$^{+/}$). **B** Correlation between energy expenditure (kcal/h) and body weight (grams). Data were evaluated in dark phase in 30-week-old male mice on a normal diet (n = 8 for WT; n = 7 for RAP250$^{+/}$). **C** Glucose oxidation profile over 24 h in 30-week-old male mice on a normal diet. Gray phase corresponds to dark phase. Data were evaluated in 30-week-old male mice on a normal diet (n = 8 for WT black symbols; n = 8 for RAP250$^{+/-}$ red symbols). **D** Brown adipose tissue weight. Data are expressed as percentage of tissue weight with respect total body weight (n = 5 for WT and n = 7 for RAP250$^{+/-}$). **E** Glucose oxidation of isolated brown adipose cells (n = 9 from 3 independent experiments performed in triplicate). **F** Brown adipose tissue paraffin slices stained with Hematoxylin/Eosin (scale bar=100 μm) and lipid droplet size quantification (**G**). Data were evaluated in 20-week-old male mice (n = 5 for WT and n = 7 for RAP250$^{+/-}$). **H** BAT sections stained with DAPI (blue), wheat germ agglutinin (WGA, green), and UCP1 (red). Scale bar 20 μm. **I** Quantification of adipocyte area and **J** quantification of UCP1 mean signal intensity (n = 3 for WT; n = 4 for RAP250$^{+/-}$). **K** Heatmaps showing gene expression modulation in transcriptomic analysis performed in BAT from 20-week-old mice (n = 3 for WT and n = 4 for RAP250$^{+/-}$). **L** Gene expression of brown adipogenic markers *Pparg2*, *Prdm16*, *Cebpa*, *Ppara*, *Dio2*, *Ppargc1* and *Ucp1* in BAT from 20-week-old mice. Data were normalized to ARP mRNA expression (n = 5 for WT, n = 7 for RAP250$^{+/-}$). Representative images for UCP1, PPARγ, C/EBPα and α-Tubulin proteins in BAT extracts (**M**) from 20-week-old mice and quantification of protein expression (**N**). Data were normalized to α-Tubulin (n = 4 for WT, n = 7 for RAP250$^{+/-}$). Data are MEAN+/− SEM. Statistical differences according to a two-sided Student´s *t* test (**A**, **D**, **E**, **G**, **I**, **J**, **L** and **N**) and Ordinary two-way ANOVA (**C**). Source data are provided as a Source Data file.

that leads to alterations in energy expenditure that resemble those detected in RAP250$^{+/-}$ mice.

Thermoneutrality reduces the enhanced energy expenditure associated with RAP250 deficiency

Next, we examined whether the metabolic profile of RAP250$^{+/-}$ mice was modified upon exposure to thermoneutral conditions, i.e., upon inactivation of BAT metabolic activity. Thus, control and RAP250$^{+/-}$ mice were housed at 30 °C for 14 weeks (starting at 8 weeks of age). Half the mice were fed a standard chow diet (TN-ND), while the other half received a HFD (TN-HFD), which enhances thermogenic activity due to the high amount of fat[34,35]. RAP250$^{+/-}$ mice subjected to thermoneutrality and a standard diet did not show alterations in body weight (Fig. 4I) or total fat mass (Fig. 4K). In contrast, RAP250$^{+/-}$ mice subjected to a HFD had a lower body weight (Fig. 4J) and a marked reduction of fat mass (Fig. 4K). Under these conditions, the weight of BAT was only reduced in RAP250$^{+/-}$ mice upon a HFD (Fig. 4L). Tissue sections revealed unaltered adipose cell size in mice on a standard diet (Fig. 4M and 4O) but a reduced adipose cell size in the RAP250$^{+/-}$ group upon treatment with a HFD (Fig. 4N and 4O). These studies provide further evidence that BAT plays a major role in the alterations in energy metabolism of RAP250$^{+/-}$ mice.

RAP250 deficiency in brown adipose tissue enhances the expression of Neuritin 1, a protein that is secreted upon catecholaminergic activation

To explore the mechanisms responsible for the enhanced metabolic activity of BAT under RAP250 deficiency, we focused on the differentially expressed gene sets detected in RNA-seq assays (Fig. S7A). Gene set enrichment analysis revealed a significant upregulation of genes involved in the action potential of neurons in RAP250-deficient BAT (Figs. 5A, and S7A), and an enhanced expression of the neurotrophic

https://doi.org/10.1038/s41467-025-62255-2

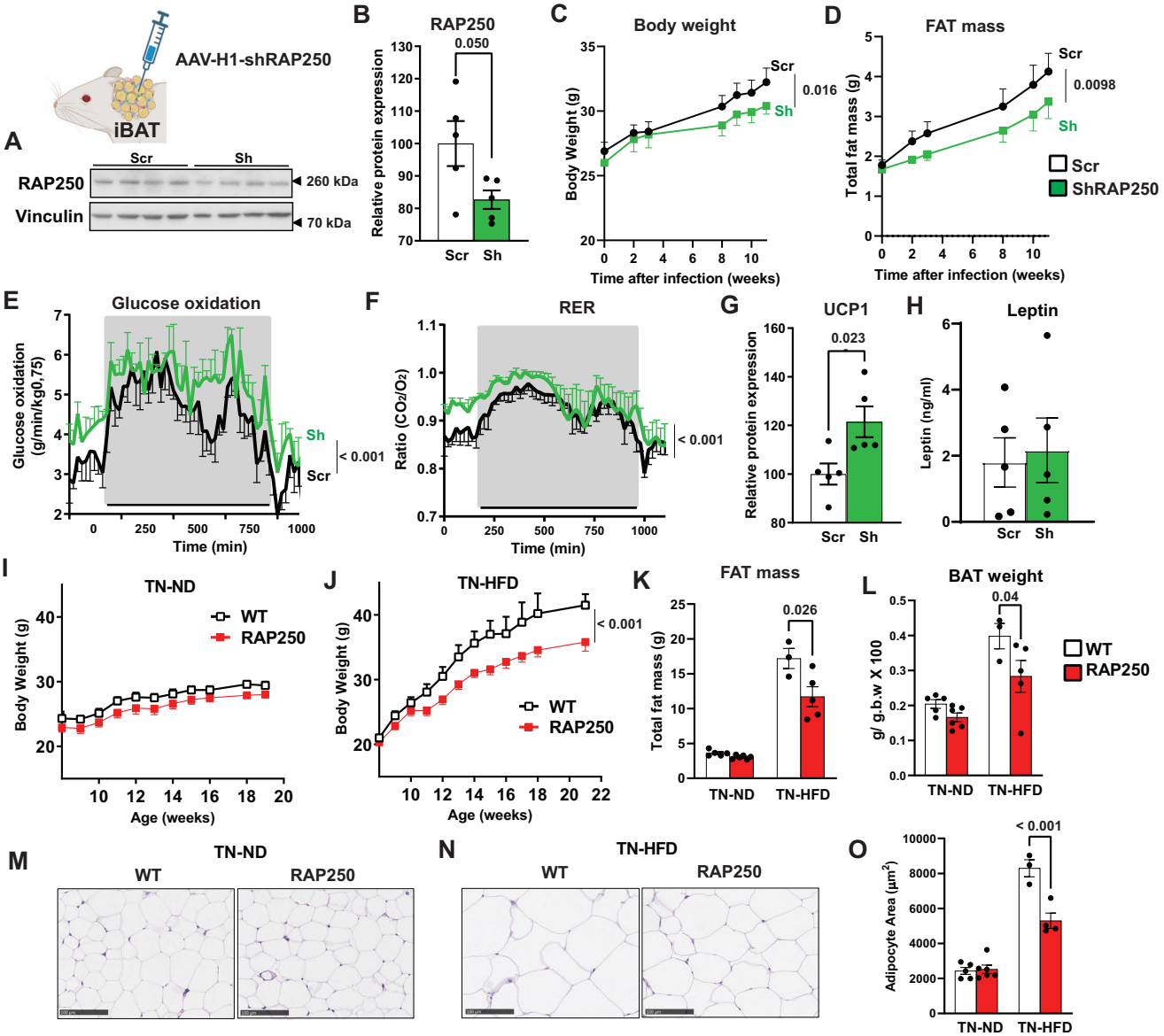

Fig. 4 | Specific RAP250 repression in BAT phenocopies many of the metabolic alterations of RAP250$^{+/-}$ mice, and thermoneutrality normalizes the metabolic alterations of RAP250$^{+/-}$ mice. Representative image for RAP250 protein expression (**A**) and quantification (**B**) in BAT extracts from 32-week-old male mice 24 weeks after injection with Scr or ShRAP250 AAVs into BAT. Data were normalized to Vinculin (n = 5 for Scr and ShRAP250). Body weight (**C**) and total fat mass (**D**) curves after AAV administration into BAT (Scr, n = 5, black symbols; ShRAP250 n = 4, green symbols). Glucose oxidation (**E**) and RER (ratio CO_2/O_2) (**F**) over 24 h in 28-week-old male mice injected with Scr or ShRAP250 AAVs into BAT and on a normal diet. Gray phase corresponds to dark phase (n = 4 for WT; n = 4 for RAP250$^{+/-}$). **G** UCP1 expression quantification in BAT extracts. Data were normalized to Vinculin (n = 5 for Scr and ShRAP250). **H** Plasma leptin from 16 h fasted mice (n = 5 for Scr and ShRAP250). Body weight curves from 8- to 22-week-old male mice subjected to thermoneutrality and on a normal chow diet (TN-ND) (**I**) or a high-fat diet (TN-HFD) (**J**). Data as grams of body weight (WT, n = 7; RAP250$^{+/-}$ n = 8 for TN-ND and WT, n = 4 and RAP250$^{+/-}$ n = 6 for TN-HFD). Black symbols for WT mice and red symbol for RAP250$^{+/-}$. **K** Total fat mass from 22-week-old mice under TN-ND and from 20-week-old mice under TN-HFD. Data as grams of FAT (WT, n = 5, RAP250$^{+/-}$ n = 6 for TN-ND and WT, n = 3, RAP250$^{+/-}$ n = 5 for TN-HFD). **L** Brown adipose tissue weight. Data are expressed as percentage of tissue weight with respect total body weight (TN-ND WT, n = 5, RAP250$^{+/-}$ n = 6; TN-HFD WT n = 3, and RAP250$^{+/-}$ n = 5). Paraffin sections of PAT stained with Hematoxylin/Eosin for TN-ND (**M**) and TN-HFD (**N**) (scale bar=100 µm). **O** PAT adipocyte cell size of TN-ND (22-week-old) and TN-HFD (20-week-old) (WT TN-ND n = 5, RAP250 TN-ND n = 6, WT TN-HFD n = 3 and RAP250 TN-HFD n = 4, from 8–10 images per mouse). Data are MEAN+/− SEM. Statistical differences according to a two-sided Student´s *t* test (B and G) and Ordinary two-way ANOVA (**C**, **D**, **E**, **F** and **J**) and two-way ANOVA followed by Sidak's multiple comparison test (**K**, **L** and **O**). **A** Created in BioRender. Bausa, O. (2025) https://BioRender.com/rdnlgxb. Source data are provided as a Source Data file.

factor Neuritin 1 (Nrn1) and not for others as *Nrg4, Ngf, Bdnf* and *S100b* (Fig. 5B). In keeping with these data, RAP250-deficient BAT showed an enhanced expression of tyrosine hydroxylase (TH), suggesting an increased sympathetic innervation[17] (Fig. 5C and D). In keeping with this, cell type deconvolution analysis of bulk transcriptomics detected an increased abundance of non-myelinated Schwann cells in RAP250-deficient BAT (Fig. 5E). This is relevant since sympathetic nerve fibers innervating BAT are predominantly non-myelinated Schwann cells, and they play a key role in neurotransmission, allowing rapid norepinephrine release to stimulate thermogenesis[36,37]. This type of analysis also revealed an increased abundance of myelinated Schwann cells in RAP250-deficient BAT (Fig. S7B).

Analysis of western blot and real-time PCR validated the increased expression of Nrn1 in RAP250-deficient BAT (Fig. 5F–H). The increased

https://doi.org/10.1038/s41467-025-62255-2

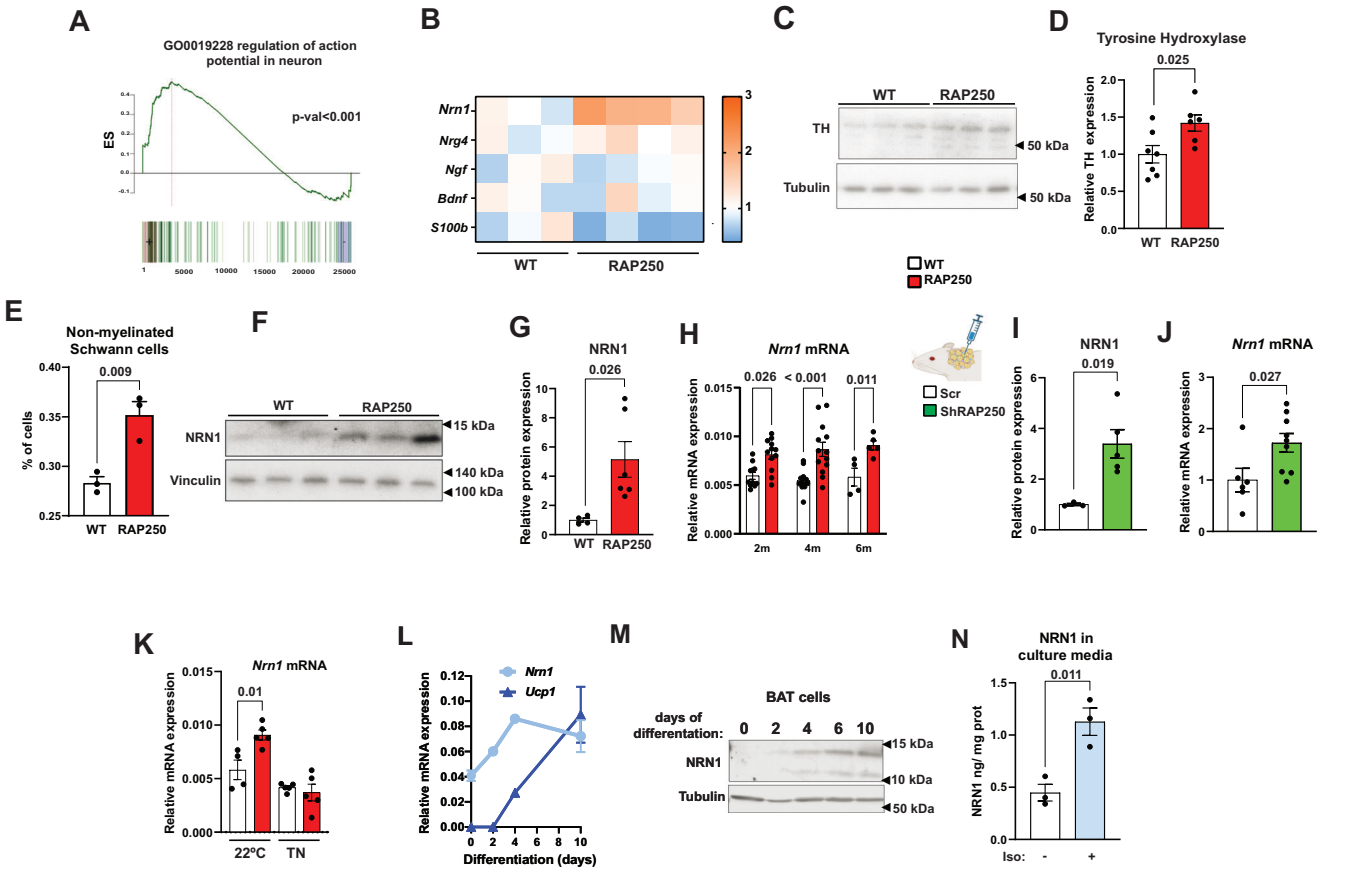

Fig. 5 | Nrn1 is highly expressed in BAT from RAP250-deficient mice, and it is secreted upon catecholaminergic activation by brown adipose cells. A Gene set enrichment analysis results of Regulation of action potential in neuron pathway (GO0019228) from Gene Ontology (GO) upregulated in BAT from RAP250$^{+/-}$ mice. **B** Heatmap of expression of specific neurotrophic and/or batokine genes in BAT from WT and RAP250 BAT (n = 3). Representative image for Tyrosine Hydroxylase (TH) expression (**C**) and quantification (**D**) in BAT extracts from 20 -week-old WT and RAP250-deficient mice (WT n = 7, RAP250$^{+/-}$ n = 6). **E** Percentage of non-myelinated Schwann cells in 20 -week-old WT and RAP250-deficient mice (n = 3). Representative image for NRN1 expression (**F**) and quantification (**G**) in BAT extracts from 20-week-old WT and RAP250-deficient mice (WT n = 4, RAP250$^{+/-}$ n = 6). **H** Nrn1 gene expression in BAT tissue from 2-, 4-, and 6-month-old WT and RAP250- deficient mice (2 m WT n = 11, RAP250$^{+/-}$ n = 12; 4 m WT n = 12, RAP250$^{+/-}$ n = 13; 6 m WT n = 4, RAP250$^{+/-}$ n = 5). NRN1protein quantification (Scr n = 3 and ShRAP250 n = 5) (**I**) and Nrn1 gene expression (Scr n = 6 and ShRAP250 n = 9) (**J**) in Scr or ShRAP250 AAVs into BAT. **K** Nrn1 gene expression in BAT from WT and RAP250-deficient mice at 22 °C and subjected to thermoneutrality (TN) (WT n = 4, RAP250$^{+/-}$ n = 5, WT TN n = 5, RAP250$^{+/-}$ TN n = 5). **L** Nrn1 and UCP1 mRNA expression during brown adipogenesis (d0 n = 3, d2 n = 2 and d4 n = 2 are from a representative experiment; for d10 n = 4 (UCP1 mRNA) and n = 6 (NRN1 mRNA) from 2 and 3 independent experiments performed by duplicate). **M** Representative image of NRN1 expression during brown adipogenesis at different days of differentiation (0, 2, 4, 6 and 10). **N** NRN1 expression in culture media from differentiated brown adipose cells under 2 hours of treatment without and with Isoproterenol (10uM). Data are expressed as total NRN1 in media (ng) corrected by total cell protein (mg) (Representative experiment performed in triplicate n = 3). Data are MEAN+/− SEM. Statistical differences according to a two-sided Student´s *t* test (**D**, **E**, **G**, **H**, **I**, **J**, **K** and **N**), and Enrichment score rotation based test (roastgsa) (**A**). Source data are provided as a Source Data file.

expression of Nrn1 mRNA was detected in BAT from RAP250$^{+/-}$ mice aged between 2 and 6 months (Fig. 5H). Nrn1 mRNA was more enriched in brown adipocytes compared to the expression detected in the stromal vascular fraction obtained from BAT, similarly to was detected for UCP1 or RAP250 (Fig. S7C–E). AAV-mediated RAP250 repression in BAT also caused an increased expression of Nrn1 mRNA and protein (Fig. 5I and J). In contrast, AAV-mediated RAP250 repression in perigonadal adipose tissue did not alter the expression of Nrn1 (Fig. S7F). Exposure of mice to thermoneutrality abrogated the stimulation of Nrn1 mRNA levels in BAT (Fig. 5K), in keeping with the absence of changes in fat mass.

In separate studies, we analyzed the expression of Nrn1 in mouse brown adipose cells during adipogenesis. Nrn1 mRNA was substantially expressed in preadipocytes and it underwent a two-fold increase in adipocytes under conditions in which UCP1 was markedly induced (Fig. 5L). In contrast, the expression of Nrn1 protein was not detectable in preadipocytes and was markedly induced during brown adipogenesis (Fig. 5M). Nrn1 was detected as 15 kDa and 12 kDa bands and it is likely that the former is an unprocessed form of the protein. Nrn1 protein was also detected in culture media from brown adipocytes, suggesting that it was secreted. Moreover, the secretion was rapidly stimulated in response to isoproterenol treatment (Fig. 5N). In all, our data indicate that Nrn1 is expressed and secreted by brown adipose cells and that its expression is markedly enhanced in response to brown adipogenesis.

Enhanced expression of Neuritin-1 in thermogenic adipose cells stimulates brown adipose tissue metabolism

We next tested whether Nrn1 expression in thermogenic adipose cells had metabolic effects in mice. To this end, control mice subjected to a normal diet were treated with AAVs encoding Nrn1 under the control of the UCP1 promoter or an empty vector. Thirty weeks after the AAV administration, AAV-Nrn1-treated mice showed a 3-fold greater expression of Nrn1 mRNA and protein in BAT whereas no changes in expression were detected in ING adipose tissue (Fig. 6A, and S8A). Plasma levels of Nrn1 were detectable but no differences were found

https://doi.org/10.1038/s41467-025-62255-2

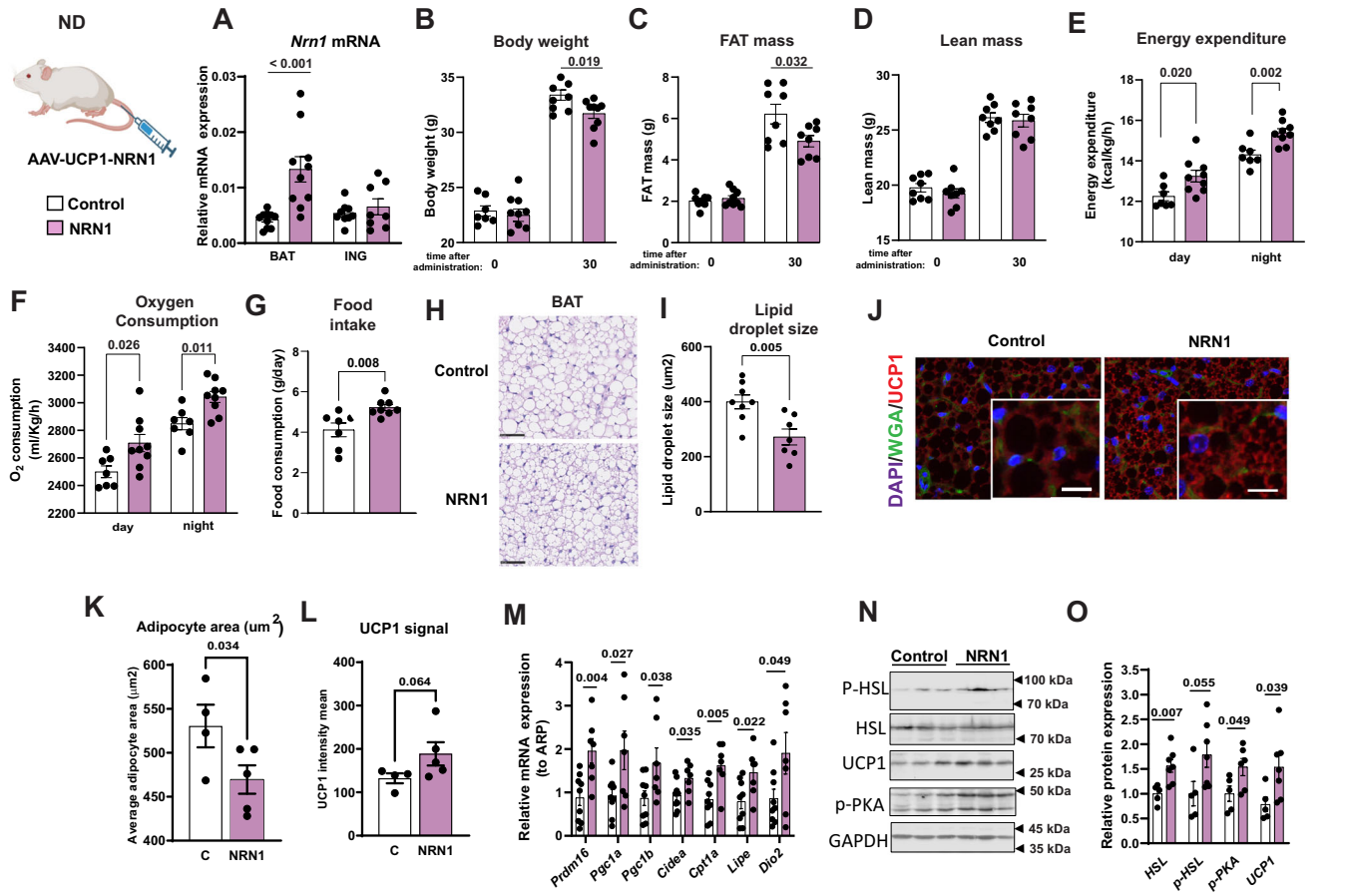

Fig. 6 | Enhanced expression of Neuritin-1 in thermogenic adipose cells stimulates brown adipose tissue metabolism. A Nrn1 gene expression in BAT and SAT from mice injected via the tail-vein with either AAV-UCP1 empty (Control) or AAV-UCP1-NRN1 vector under UCP1 promoter (BAT AAV-Control n = 9; BAT AAV-UCP1-NRN1 n = 7; SAT AAV-Control n = 8, SAT AAV-UCP1-NRN1 n = 6). Body weight (time 0 Control n = 7 and NRN1 n = 10; time 30 Control n = 9 and NRN1 = 9) (**B**), total fat mass (n = 8) (**C**) and lean mass (n = 8) (**D**) graphs for mice before administration of an AAV Control or AAV-UCP1-NRN1 at time 0 (8-week-old mice) and 30 weeks after administration. Energy expenditure (**E**) and oxygen consumption (**F**) graphs during day and night periods in mice injected with AAV-Control or AAV-UCP1-NRN1 protein 26 weeks after infection (AAV-Control n = 7; AAV-UCP1-NRN1 n = 9). **G** Food intake as grams of daily intake in mice infected with AAV-control and AAV-UCP1-NRN1 (AAV-Control n = 7; AAV-UCP1-NRN1 n = 9). Brown adipose tissue paraffin slices stained with Hematoxylin/Eosin (**H**) (scale bar=100 μm) and lipid droplet size quantification (**I**). Data were evaluated 30 weeks after infection for Control and overexpressing NRN1 under UCP1 promoter mice (AAV-Control n = 8; AAV-UCP1-NRN1 n = 7). **J** BAT sections stained with DAPI (blue), wheat germ agglutinin (WGA, green), and UCP1 (red). Scale bar 20 μm. **K** Quantification of adipocyte area and (**L**) of UCP1 mean signal intensity (n = 4 for AAV-Control; n = 5 for AAV-UCP1-NRN1). **M** Gene expression for *Prdm16, Ppargc1a, Ppargc1b, Cidea, Cpt1a, Lipe* and *Dio2* in BAT 30 weeks after AAV infection with Control or NRN1 under the UCP1 promoter. Data were normalized to ARP mRNA (n = 9 for AAV-Control; n = 7 for AAV-UCP1-NRN1). Representative images for p-HSL, HSL, UCP1, proteins phosphorylated by PKA substrates (p-PKA) and GAPDH proteins in BAT extracts 30 weeks after AAV infection with Control or NRN1 under the UCP1 promoter (**N**) and quantification (**O**). Data were normalized to GAPDH expression (n = 6 for AAV-Control; n = 7 for AAV-UCP1-NRN1). Data are MEAN+/− SEM. Data are MEAN+/− SEM. Statistical differences according to a two-sided Student´s *t* test for all figures except one-sided Student´s *t* test (**K** and **L**). **A** Created in BioRender. Bausa, O. (2025) https://BioRender.com/rdnlgxb. Source data are provided as a Source Data file.

between control and Nrn1-treated groups (Fig. S8B). Under these conditions, AAV-Nrn1-treated mice showed a lower body weight and lower fat mass (Fig. 6B and C) in the absence of alterations in lean mass (Fig. 6D). Energy expenditure, oxygen consumption, CO_2 production and glucose oxidation were enhanced in AAV-Nrn1-treated mice (Fig. 6E, F, S8C and D). Under these conditions, food intake but not ambulation was enhanced (Fig. 6G, and S8E). AAV-Nrn1-treated mice showed lower concentrations of plasma triglycerides, normal glycemia, and a trend for reduced leptin levels (Fig. S8F–H).

Sections of BAT revealed reduced size of brown adipose cells and lipid droplets upon Nrn1 treatment (Fig. 6H, and I). Triple staining of BAT section showed a reduced adipose cell size in BAT from Nrn1-treated mice (Fig. 6J and K). In addition, an increased abundance of UCP1 in brown adipocytes from Nrn1 mice was also detected (Fig. 6J and L). In all, these data suggest an enhanced BAT metabolism and thermogenesis upon Nrn1 expression.

In keeping with this view, we detected an increased expression of thermogenic and metabolic genes in the AAV-Nrn1-treated group (Fig. 6M), and also an enhanced expression of phosphorylated HSL, active PKA, UCP1 (Fig. 6N and O). We also detected that chronic overexpression of Nrn1 in brown adipocytes enhanced the expression of OXPHOS subunits relevant in respiratory complexes I and II but not for CV (Fig. S8I and J). The Nrn1 group also showed a reduction in adipose cell size in visceral and subcutaneous depots (Fig. S8K and L).

Mice subjected to a HFD were also treated with AAVs encoding Nrn1 under the control of the UCP1 promoter or an empty vector. Nrn1-treated mice showed increased Nrn1 gene expression in BAT and ING adipose tissue (Fig. 7A), and no differences in plasma levels were detected between groups (Fig. S9A). AAV-Nrn1-treated mice showed a lower rate of body weight and fat mass gain compared to control mice (Fig. 7B and C) in the absence of alterations in lean mass (Fig. S9B). Energy expenditure, oxygen consumption, and lipid oxidation were

https://doi.org/10.1038/s41467-025-62255-2

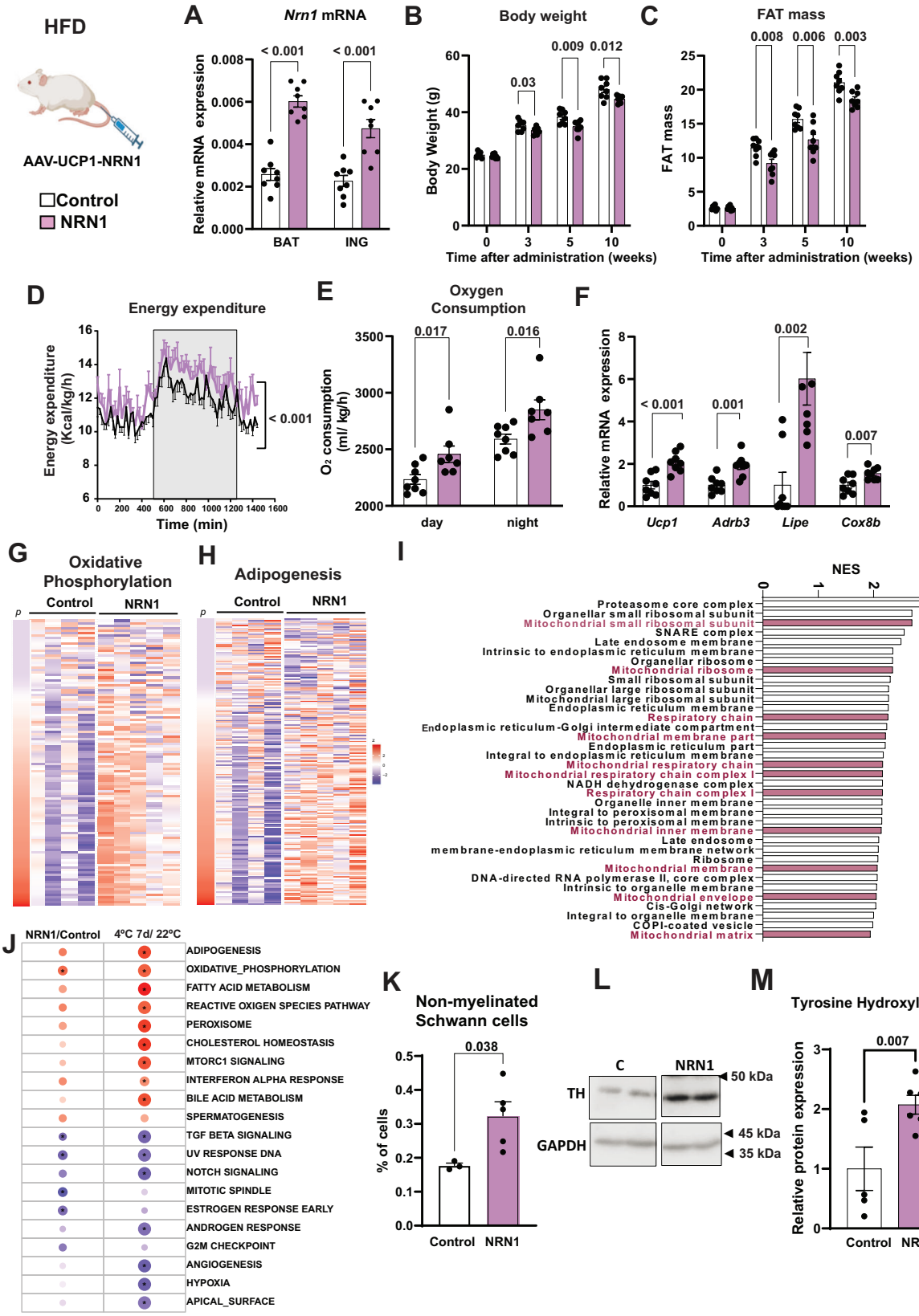

enhanced in AAV-Nrn1-treated mice (Fig. 7D, E, and S9C). Under these conditions, food intake was not altered (Fig. S9D), and nocturnal ambulation was enhanced in these mice (Fig. S9E). These mice showed lower concentrations of plasma triglycerides and leptin, and normal glycemia (Fig. S9F–H). We also detected an enhanced expression of thermogenic and metabolic genes in the Nrn1 group (Fig. 7F).

Neuritin 1 induces a thermogenic program in BAT

As we found that enhanced Nrn1 expression activates brown adipose tissue, we next analyzed the mechanisms involved. To this end, we performed RNA-Seq assays using BAT samples from AAV-Nrn1-treated and control mice. 218 genes were significantly upregulated and 249 were downregulated by Nrn1 expression ($p < 0.01$). Gene set

Fig. 7 | Enhanced expression of Neuritin-1 in thermogenic adipose cells protects from HFD, promotes upregulation of many mitochondrial proteins and show similarity to the effects caused by chronic cold exposure. A Nrn1 mRNA expression in BAT and SAT in mice injected via the tail-vein with either AAV Control or NRN1 vector under UCP1 promoter and subjected to a HFD for 15 weeks (AAV-Control n = 8, black symbols; AAV-UCP1-NRN1 n = 8, violet symbols). Body weight (**B**) and total fat mass (**C**) graphs for mice before administration of an AAV Control or NRN1 under the UCP1 promoter (AAV-UCP1-NRN1) at time 0 (8-week-old mice) and 3, 5, and 10 weeks after administration under HFD conditions (AAV-Control n = 8; AAV-UCP1-NRN1 n = 8). **D** Energy expenditure over 24 h in male mice infected with AAV empty vector or NRN1 under UCP1 on a HFD 13 weeks after administration. Gray phase corresponds to dark phase (AAV-Control n = 8; AAV-UCP1-NRN1 n = 7). **E** Oxygen consumption graph during day and night period in mice injected with AAV Control or AAV-UCP1-NRN1 (AAV-Control n = 8; AAV-UCP1-NRN1 n = 7). **F** Gene expression of *Ucp1, Adrb3, Lipe and Cox8b* in BAT 15 weeks after AAV infection with Control or NRN1 under the UCP1 promoter. Data were normalized to ARP mRNA (AAV-Control n = 8; AAV-UCP1-NRN1 n = 8). **G** and **H** Heatmaps showing z-scores of gene expression levels for Oxidative Phosphorylation (**G**) and Adipogenesis (**H**) Hallmarks in BAT from mice subjected to a normal diet infected with AAV empty vector or NRN1 under the control of the UCP1 promoter (n = 4 for Control and n = 5 for AAV-UCP1-NRN1). Color indicates (red: positive expression and blue: negative expression versus Control). Column *p* shows fold changes for individual genes. **I** Normalized scores of gene set enrichment analysis of top GO terms (Cellular Compartment) upregulated in BAT from mice AAV-NRN1 treated mice (adj. pval<0.05). In purple color, mitochondrial related pathways are shown. **J** Bubble chart of gene set enrichment analysis results showing pathways modified in response to NRN1 overexpression and upon cold exposure. Color indicates Normalized Enrichment Score (red: positive NES, blue: negative NES). Stars indicate p-value lower than 0.05. **K** Percentage of non-myelinated Schwann cells obtained by deconvolution analysis comparing control versus AAV-NRN1 treated mice in ND (AAV-Control n = 3; AAV-UCP1-NRN1 n = 5). Tyrosine Hydroxylase expression (**L**) and quantification (**M**) in BAT extracts from control and AAV-NRN1 treated mice in ND (AAV-Control n = 5; AAV-UCP1-NRN1 n = 7). Data are MEAN+/− SEM. Data are MEAN+/− SEM. Statistical differences according to a two-sided Student´s *t* test (**A**–**F**, **K** and **M**). In figure J the bubble size indicates statistical significance (bigger = lower adjusted P value). Inner asterisk indicates adjusted P value < 0.05. Source data are provided as a Source Data file.

enrichment analysis revealed enhanced abundance of Hallmark Oxidative Phosphorylation, and Adipogenesis pathways in response to chronic NRN1 (Fig. 7G and H). Analysis of GO Cellular Compartment GSEA revealed that most of the genes upregulated were mitochondrial (encoding for mitochondrial proteins) (Fig. 7I). The pattern of changes detected upon NRN1 expression was similar to the changes reported in response to cold exposure to 4 °C for 1 week[38]. Our data indicate that BAT oxidative metabolism is activated upon NRN1 overexpression, and that the effects of NRN1 show striking similarity to the effects caused by chronic cold exposure (Fig. 7J). These data indicate the existence of common processes operating in Nrn1 overexpressing BAT and upon cold exposure.

We performed cell type deconvolution analysis of bulk transcriptomics from control and Nrn1 overexpressing BAT tissues, and we detected and increased abundance of non-myelinated Schwann cells (Fig. 7K), which was parallel to an increased expression of tyrosine hydroxylase (Fig. 7L and M). Moreover, a reduced abundance of myelinated Schwann cells was also detected (Fig. S9I). In all, these data indicate a sympathetic remodeling in BAT by Nrn1 involved an increased proliferation of non-myelinated Schwann cells.

Neuritin 1-deficient brown adipose cells show a reduced metabolic response to isoproterenol

To further analyze whether Nrn1 has metabolic effects in brown adipocytes, we repressed Nrn1 in primary brown preadipocytes using lentiviruses encoding shRNA (Fig. 8A). These cells showed a normal differentiation and the expression of protein markers such as $PPAR_{\gamma 2}$, $PPAR_{\gamma 1}$, UCP1 and HSL was indistinguishable from that observed in control adipocytes (Fig. 8B and S9J). Given these observations, we monitored the acute stimulatory response of brown adipocytes to the β-adrenergic receptor agonist isoproterenol[39]. Isoproterenol activated the phosphorylation of HSL and other PKA substrates in control brown adipocytes (Fig. 8C–E). This activation was markedly reduced in Nrn1-deficient brown adipocytes (Fig. 8C–E). Isoproterenol also induced crucial genes, such as *Ppargc1a* and *Ucp1*, in control cells (Fig. 8F, and G). This process was largely repressed in Nrn1-deficient cells (Fig. 8F and G). We also analyzed the effects of Nrn1 deficiency on mitochondrial respiration in brown adipocytes. In control brown adipocytes, mitochondrial respiration was reduced upon addition of oligomycin, and isoproterenol increased mitochondrial respiration to values close to those measured in the presence of FCCP (maximal respiration) (Fig. 8H). Depletion of Nrn1 reduced the effects of isoproterenol on mitochondrial respiration, and also maximal mitochondrial respiration (Fig. 8H). Under these conditions basal respiration or ATP-coupled respiration were unaltered in Nrn1-deficient cells (Fig. 8I). The reduced response to isoproterenol was not a consequence of changes in the expression of β3-adrenergic receptors (Fig. 8J and K). In all, these results indicate that Nrn1 protein is synthesized by brown adipocytes and that it can modulate the metabolism of brown adipocytes and their capacity to respond to catecholamines.

Exogenous Neuritin 1 stimulates metabolism in brown adipocytes

To analyze whether extracellularly present Nrn1 has metabolic effects in brown adipocytes, we have expressed and purified mouse recombinant NRN1 to homogeneity (Fig. 8L). Next, we incubated brown adipocytes with recombinant NRN1 (100 ng/ml). Short-term incubation with recombinant NRN1 enhanced the phosphorylation of protein kinase A (PKA) substrates in brown adipocytes (Fig. 8M). In addition, NRN1 caused a marked induction of *Ucp1* and *Ppargc1a* gene expression in brown adipocytes (Fig. 8N and O). NRN1 also increased the effects of isoproterenol on mitochondrial respiration (Fig. 8P). Long-term incubation of brown adipocytes with NRN1 enhanced the expression of NDUFB8 subunit of the respiratory complex I (Fig. 8Q and R). These results clearly reveal a thermogenic effect of extracellular NRN1 in brown adipocytes, and further suggest that NRN1 has the capacity to act as an autocrine/paracrine factor in brown adipose tissue.

Discussion

The results reported here support the following highlights: a) RAP250 protein is a key component of energy homeostasis and it modulates BAT metabolism; b) RAP250 deficiency in brown adipose cells induces the expression of Nrn1, a factor until now unknown as a regulator of BAT biology; c) AAV-mediated overexpression of Nrn1 in brown adipose cells improves energy expenditure and stimulates BAT metabolism; d) Nrn1 repression disrupts the metabolism of brown adipocytes, an observation that indicates an autonomous cellular response; and e) exogenous mouse recombinant NRN1 enhances the activity of protein kinase A, stimulates mitochondrial respiration and induces the expression of thermogenic genes in brown adipocytes, supporting the view that NRN1 acts as a secreted factor in brown adipose tissue.

Our findings reveal that RAP250 plays a key role in maintaining energy metabolism and adiposity in mice. We demonstrate that RAP250 deficiency upregulates energy metabolism, reduces adiposity, and enhances insulin sensitivity in mice. In addition, we found that global RAP250 deficiency in these animals stimulates BAT metabolism and that local AAV-mediated RAP250 repression in BAT reduces adiposity and enhances global glucose oxidation and BAT UCP1 expression. In addition, we document that RAP250 expression is

https://doi.org/10.1038/s41467-025-62255-2

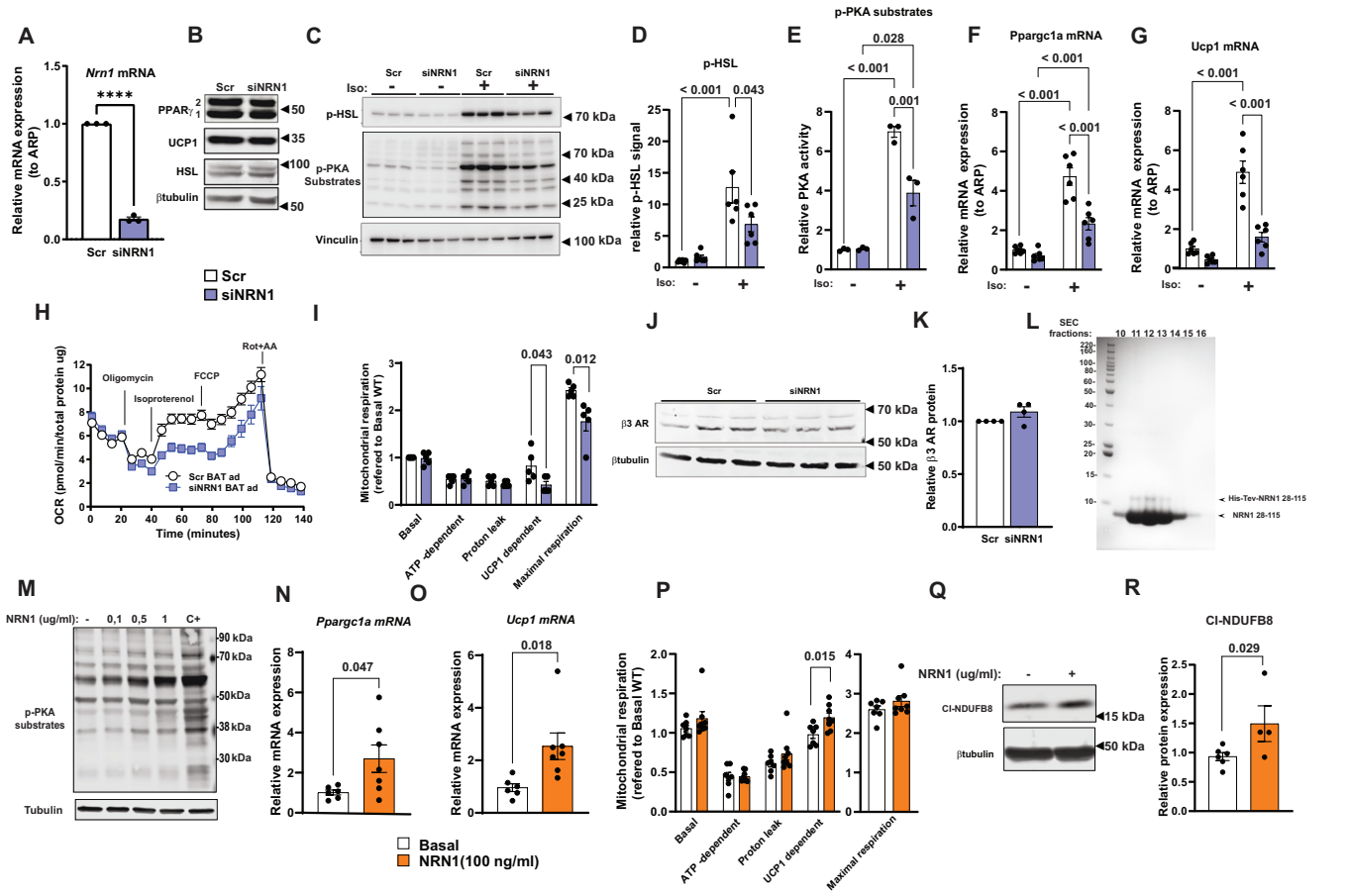

Fig. 8 | Neuritin1-deficient brown adipose cells show a reduced metabolic response to isoproterenol, diminished maximal respiration and mouse recombinant NRN1 protein promotes PKA activation and induction of CI-NDUFB8 respiratory subunit. A Relative Nrn1 mRNA expression in Scr and siNRN1 preadipocytes. Data are from 3 separate differentiation experiments. **B** Representative imatge of PPARγ1 and γ2, UCP1, HSL and β-tubulin expression in Scr and siNRN1 brown adipocytes at day 10 of differentiation. p-HSL and phosphorylated by PKA substrates (p-PKA) expression (**C**) and quantification (**D** and **E**) in Scr and siNRN1 adipocytes (day 10 of differentiation), in basal and treated with Isoproterenol (10 μM) for 2 h (p-HSL n = 6 from 2 experiments performed in triplicate (p-HSL) and n = 3 from 1 representative experiment performed in triplicate (p-PKA)). *Ppargc1a* mRNA (**F**) and *Ucp1* mRNA (**G**) expression in Scr and siNRN1 adipocytes cells, in basal and treated with isoproterenol (10 μM) for 2 h. Data are mean of 2 experiments performed in triplicate. **H** Seahorse representative experiments for Scr and siNRN1 brown adipocytes at day 10 of differentiation (Scr n = 4 and siNRN1 n = 5). **I** Mitochondrial respiration values referred to basal WT. Data are the mean of 5 independent experiments. **J**, **K** Expression (**J**) and quantification (**K**) of β3 Adrenergic Receptors in Scr and siNRN1 brown adipocytes at day 10 of differentiation. Data are mean of 4 independent experiments. **L** NRN1 SEC fractions run on 10% Bis-Tris NuPAGE Midi SDS-PAGE gels with MES running buffer. BenchMark protein markers (Invitrogen) were included for reference. **M** Abundance of PKA phosphorylated substrates (p-PKA) in brown adipocytes treated with 0.1, 0.5 and 1 μg/ml of recombinant NRN1 protein. **N**, **O** *Ppargc1a* (**N**) and *Ucp1*(**O**) mRNA expression in adipocytes treated with NRN1 (100 ng/ml) during 2 hours (n = 6 from 3 independent experiments). **P** Mitochondrial respiration values referred to basal WT respiration in untreated brown adipocytes non-treated (white bars) and cells treated with NRN1 at a concentration of 100 ng/ml (orange bars) from day 4 of differentiation (Representative experiment, Basal n = 7 and NRN1 treated adipocytes n = 8). **Q**, **R** Expression (**Q**) and quantification (**R**) of CI-NDUFB8 subunit in Scr adipocytes cells treated chronically with NRN1 (100 ng/ml) from day 4 of differentiation until day 10. Data are the mean of 3 independent experiments. Data are MEAN+/− SEM. Statistical differences according to a two-sided Student´s *t* test (**A**, **I**, **K**, **N**, **O, P** and **Q**) and two-way ANOVA followed by Sidak's multiple comparison test (**D**–**F** and **G**). Source data are provided as a Source Data file.

markedly attenuated in BAT in response to cold, and is also reduced in brown adipocytes by phosphodiesterase inhibitors suggesting a regulatory role of cAMP. Based on all these data, we propose that RAP250 regulates energy metabolism, most likely through the modulation of the metabolic activity of BAT. In keeping with these data, many common variants of RAP250 show a very strong association with hip circumference-adjusted BMI (https://t2d.hugeamp.org/gene.html?gene=NCOA6)[40] (Fig. S9). This observation points to the participation of RAP250 in human metabolism.

Our data indicate that RAP250 deficiency causes leanness in mice as a result of increased BAT metabolism and energy expenditure. We are aware of different studies indicating that

RAP250 plays a key role in white adipogenesis under in vitro conditions[27]. Thus, the transcriptional activity of PPARγ is impaired in RAP250 KO mouse embryo fibroblasts[27,41,42], and these cells are refractory to PPARγ-stimulated adipogenesis[27]. Future studies are required to proof that RAP250 indeed controls in vivo white adipogenesis. RAP250 also regulates liver metabolism, and its inactivation disrupts hepatic lipid metabolism and gluconeogenesis, leading to enhanced insulin sensitivity[23,24,43]. This combined set of changes explains the phenotype of RAP250-deficient mice, namely reduced gain of adiposity and lack of ectopic fat deposition in tissues under conditions of nutritional overload.

The enhanced energy expenditure of RAP250$^{+/-}$ mice was linked to greater glucose oxidation under a normal diet and to increased lipid oxidation upon HFD conditions. Moreover, these animals showed an enhanced BAT metabolism that was characterized by large transcriptomic alterations, increased glucose oxidation, improved mitochondrial respiration, high expression of key genes *Pparg2, Prdm16, Cebpa, Ppara, Ppargc1a, Ucp1* and *Dio2*, and increased expression of

proteins UCP1, PPARγ and C/EBPα. Two additional experimental findings revealed that BAT plays a major primary role in the metabolic changes detected in RAP250-deficient mice. Thus, local repression of RAP250 protein mediated by the injection of AAV shRAP250 particles into the interscapular BAT depot of wild-type mice phenocopied many of the metabolic changes detected in RAP250-deficient mice, including reduced body weight, lower fat mass, and enhanced glucose oxidation. These effects were specific to RAP250 repression in BAT, because a similar genetic manipulation of RAP250 in PAT did not have metabolic consequences. A second observation came from the exposure of RAP250-deficient mice to thermoneutrality, which inactivates BAT thermogenesis. Under these conditions, marginal or no differences in body weight, fat mass or glucose tolerance were detectable between control and RAP250$^{+/-}$ mice. Moreover, the combination of thermoneutrality and a HFD, the latter enhancing the thermogenic activity of BAT[35,44], maintained the differences in body weight, fat mass, and glucose tolerance normally appearing in RAP250-deficient mice. In all, our data strongly support the view that RAP250 modulates energy expenditure through the regulation of BAT activity in such a way that primary changes in BAT function lead to alterations in adiposity.

Neuritin 1 (Nrn1), originally termed candidate plasticity-related gene 15 or Cpg15, was identified as a gene induced by the glutamate analogue kainate in the hippocampus dentate gyrus[30]. Nrn1 is a glycosylphosphatidylinositol (GPI)-anchored neuropeptide expressed in postmitotic neurons and it regulates synaptic plasticity, neurite growth, and neuronal migration and survival[29,31,32,45–47]. It is also involved in memory and learning[48]. Moreover, Nrn1 operates in cells other than neurons. In this regard, it is also produced by follicular regulatory T cells, and it acts on B cells to suppress autoantibody development against tissue-specific antigens[49]. In addition, this protein is expressed in tissues such as the placenta, lung and spleen[50]. In this study, we have identified that Nrn1 is synthesized in BAT and induced in RAP250-deficient conditions. Our data support the notion that Nrn1 plays a key role in BAT metabolism.

In this study, we document that Nrn1 is upregulated in BAT under conditions of RAP250 deficiency. Given the observation that Nrn1 is upregulated in BAT upon local AAV-mediated RAP250 repression, we support the notion that RAP250 locally modulates Nrn1 gene expression in BAT. Moreover, we document that Nrn1 is abundantly expressed in brown adipocytes and that its expression is regulated during differentiation state at translational or post-translational levels. As RAP250 participates in COMPASS-related complexes containing the H3K4 methyltransferases MLL3 and MLL4[20,21,51], we propose that RAP250 repression drives epigenetic changes, thus causing an enhanced expression of Nrn1. The intricacy of those complexes is high, and MLL3 and MLL4 induce monomethylation of H3K4 at enhancer regions, whereas another enzyme in MLL3 and MLL4 COMPASS, namely UTX, demethylates H3K27me3, a modification associated with transcription repression by the Polycomb group of proteins[52,53].

Here, we also demonstrate that Nrn1 expressed in brown adipose cells causes the local activation of BAT metabolism and thermogenesis. Thus, the expression of Nrn1 in thermogenic adipose cells causes the activation of energy expenditure under normal conditions or upon an HFD. Under these conditions, we also detected a reduction in body weight gain. This occurred in parallel to an enhanced expression of BAT metabolic genes, including *Prdm16, Ppargc1a, Cidea, Cpt1a, Hsl*, and *Dio2*. RNA-Seq assays revealed the existence of a metabolic reprogramming in response to chronic NRN1 expression in BAT characterized by the induction of mitochondrial genes and also genes relevant in adipose cell differentiation. The pattern of changes detected upon NRN1 expression was similar to the changes reported in response to cold exposure to 4 °C for 1 week[38]. In all, these data indicate that BAT oxidative metabolism is activated upon NRN1 overexpression, and that the effects of NRN1 show striking similarity to the effects caused by chronic cold exposure.

The effects of Nrn1 in BAT seem to be largely local. In this regard, the changes in energy expenditure or in BAT gene expression detected upon overexpression of Nrn1 in BAT occurred in the absence of alterations in the plasma levels of Nrn1. At a cellular level, Nrn1 seems to operate through an autocrine/paracrine mode of action. In this context, we detected that Nrn1 is secreted from brown adipocytes and that this secretion is significantly enhanced in the presence of the β-adrenergic receptor agonist isoproterenol. In addition, we found that Nrn1 repression in brown adipose cells does not alter differentiation, but it markedly reduces the response to isoproterenol. Nrn1 groups with local-acting factors, such as BMP8b, which are secreted by brown adipocytes and activate BAT metabolism[16,54]. Interestingly, some common variants of the Nrn1 gene show a very strong association with BMI (https://t2d.hugeamp.org/gene.html?gene=NRN1), which suggests that Nrn1 participates in human metabolism.

Interestingly, incubation of brown adipocytes with mouse recombinant NRN1 enhances the activity of protein kinase A, stimulates mitochondrial respiration, and induces the expression of thermogenic genes in brown adipocytes, supporting the view that NRN1 acts as a secreted factor in brown adipose tissue. The specific receptors for NRN1 have not been definitively identified. To date, no canonical, high-affinity cell surface receptor has been unequivocally demonstrated[55]. Moreover, NRN1 is not part of a known ligand family like neurotrophins or FGFs, and it does not display any conserved domain homologous to these or other classical signaling molecules[56]. Several studies have proposed indirect mechanisms or potential receptor candidates for NRN1. For instance, cross-talk between NRN1 and insulin signaling has been observed, suggesting that neuritin may enhance or depend on insulin receptor pathways for its effects[57]. Notably, pharmacological blockade of the insulin receptor, but not the insulin-like growth factor 1 receptor, abrogated these effects, indicating a specific involvement of the insulin receptor in neuritin signaling. In addition, there is evidence that neuritin interacts with fibroblast growth factor receptor 1 (FGFR1) to mediate axonal branching in granule neurons. Immunoprecipitation assays have revealed a strong association between neuritin and FGFR1, and inhibition or knockdown of FGFR1 significantly suppressed neuritin-induced axonal branching, suggesting that FGFR1 plays a critical role in neuritin's effects on neuronal development[58]. Regarding downstream signaling, activation of the ERK/MAPK and PI3K/Akt pathways has been observed following neuritin 1 treatment, consistent with its role in promoting cell survival and growth[57,59]. It is also likely that Nrn1-receptor complex undergoes internalization, which may be relevant in further signaling[49].

In our study, we further demonstrate that neuritin 1 can rapidly activate protein kinase A signaling in brown adipocytes. Altogether, these findings suggest that neuritin 1 acts pleiotropically, modulating multiple pathways depending on the cellular context. However, the precise molecular mechanisms underlying its actions remain to be fully elucidated and warrant dedicated investigation.

On the basis of our findings, we conclude that Nrn1 is a key regulator of brown adipocytes, it performs trophic actions, and it preserves the capacity to respond to catecholamines, a crucial physiological characteristic of brown adipocytes. We do not exclude the possibility that Nrn1 exerts a neurotropic action in BAT. In fact, Nrn1 overexpression caused an increased tyrosine hydroxylase expression and enhanced abundance of non-myelinated Schwann cells in BAT, supporting a role on sympathetic innervation in this tissue. Given the properties of Nrn1, it emerges as a potentially useful protein for targeting energy expenditure in humans.

Methods

Animal care and diet treatment

RAP250 heterozygous mice, with a null mutation in the *RAP250* gene, were used in this study[42]. Briefly, exons 7 and 8 were replaced with the

neo gene which is flanked by a 5-kb homologous region on each side[42]. All animal work was conducted following the guidelines established by the Animal Care Committees of the "Parc Científic de Barcelona" and the University of Barcelona.

Heterozygous female mice were crossed either with C57BL/6J male or heterozygous male mice to obtain control and heterozygous littermates. Mice were kept under a 12 h dark/light cycle and provided a standard chow diet and water ad libitum. For the high-fat diet (HFD) experiments, 10-week-old male mice were fed a standard diet or HFD for 15–20 weeks (10% or 60% calories from fat, D12492 and D12450B; Research Diets, New Brunswick, NJ, USA). Animals were fasted for 16 h (17:00–9:00) in glucose tolerance and glucose turnover tests. In thermoneutrality experiments, 8-week-old mice were kept for 22 weeks at 30 °C either under a standard chow diet or HFD. Mice were kindly gifted by the Mouse Mutant Core Facility at IRB Barcelona.

At the times indicated in figure legends, the mice were anesthetized with isoflurane and euthanized by cervical dislocation. Interscapular BAT (BAT), Perigonadal Adipose Tissue (PAT), Inguinal adipose tissue (ING), liver, gastrocnemius and heart were collected and used for RNA purification, protein extraction, or histology. Plasma was obtained by cardiac punction. All animal experiments were done in compliance with the guidelines established by the Institutional Animal Care and Use Committee of the Barcelona Science Park and University of Barcelona (Protocol number 9279, approved by the Department of Territory and Sustainability, General Directorate of Environmental Policies and the Natural Environment, Government of Catalonia).

Administration of AAV vectors

Single-stranded AAV9-Scr-RSV-GFP and AAV9-Sh RAP250-RSV-GFP vectors were generated and produced by the "Unitat de Producció de Vectors" (www.viralvector.eu) at the UAB. The sequence used to repress RAP250 was 5′-ACACATACCTCAGAACATA-3′. AAV-UCP1 empty and AAV-UCP1-Nrn1 vectors were generated by Vector Biosystems and produced by "Unitat de Producció de Vectors" at the UAB. The Vector plasmid pAAV-UCP1-m-Nrn1 contains the mouse Neuritin 1 (1-142Aa) including the signal peptide and C-terminal GPI.

The AAV9-Scr-RSV-GFP and AAV9-Sh RAP250-RSV-GFP vectors were administered as reported[60]. For BAT infection, 1×10^{10} of the total viral genome (vg) of AAV9 Scr or Sh was administered (4 × 10 µl of viral solution) per BAT depot to 8-week-old male mice. For PAT infection, 1×10^{11} of the total vg of AAV9 Scr or Sh was administered (50 µl of viral solution) to each PAT depot of 10-week-old male mice.

In Nrn1 protein overexpression experiments, 1.5×10^{12} of the total viral genome (vg) was intravascularly administered (by tail) to 8-week-old C57BL6J male mice. For HFD experiments, the diet was changed the day after the infection.

Food intake measurements

Mice were placed individually in metabolic cages and acclimatised for 24 h before measuring food intake over four consecutive days. Feeding was accessed by evaluating the food remaining in a 24-h period.

In vivo metabolic measurements

Blood samples were collected between 10:00 and 12:00 either after an overnight fast or under fed conditions; they were obtained by tail vein snip of unrestrained mice. Plasma was immediately separated by centrifugation at 4 °C and stored at −80 °C until assay. Plasma insulin and leptin levels were determined using the UltraSensitive Mouse Insulin Elisa Kit and Mouse Leptin Elisa Kit (Crystal Chem Inc., Downers Grove IL, USA); adiponectin with the Quantikine Adiponectin kit (R&D Systems, Minneapolis, USA); and cholesterol and triglycerides with BioSystems Kits (Costa Brava, Spain). Blood glucose was assayed with an Accu-Chek glucose monitor and reactive strips (Roche Diagnostics Corp.) directly in blood drops from conscious mice.

Glucose tolerance tests

were performed as described in ref. 61. Blood was collected, and glucose and insulin concentrations were measured at different time points.

Glucose turnover studies

The mice were fasted for 6 h before the infusions. The animals were connected to the infusion apparatus 2 h before the start of the infusions and had free access to water. Whole-body glucose utilization rate was determined under euglycemic-hyperinsulinemic conditions. Under physiological hyperinsulinemic conditions, insulin was infused at a rate of 4 mU/kg·min for 3 h, and D-[^{3}H]3-glucose at a rate of 30 µCi/kg·min. Throughout the infusion, blood glucose was determined from blood samples (3.5 µL) collected from the tip of the tail vein with a blood glucose meter when needed. Euglycemia was maintained by periodically adjusting a variable infusion of 10% or 16.5% glucose. Plasma glucose concentrations and D-[^{3}H]3-glucose-specific activity were determined in 5 µL of blood sampled from the tip of the tail vein every 10 min during the last hour of the infusion, as reported[62].

Non-invasive microCT scan studies

Mice were anesthetized with Ketamine/Xylazine by i.p. injection and positioned face down, with both legs fully extended, in a SkyScan 1076 high-resolution micro-CT scanner (SkyScan, Kontich, Belgium) mouse bed. 360° scans of the abdominal region were made at a rotation step of 0.8° and an isotropic voxel size of 35 µm; Source 50 kV/200 µA and 1.0 mm aluminium filter. Scans were reconstructed and analyzed using the NRecon and CTAn software provided by SkysScan. The region of interest (ROI) for each animal was defined based on skeletal landmarks from the gray-scale reconstructed images (between femoral head and L5 vertebra). Data are expressed as percentage of fat on a ROI: Fat Volume/ Total ROI Volume X 100[63]. Fat mass was also measured using magnetic resonance with EchoMRI™ Body Composition Analyzer.

Assessment of oxygen consumption in mice by indirect calorimetry

An indirect calorimetry system (Oxymax, Columbus Instruments) was used to measure oxygen consumption (VO_2), CO_2 production (VCO_2), and ambulation. The experiment included two days of acclimation and a third day (24 h) of valid data recording. Average RER index (VCO_2 ml/h produced/VO_2 ml/h consumed); Energy Expenditure (Kcal/h/Kg) [defined as VO_2x(3.815 + 1.232xRER)/1000]; Glucose Oxidation (g/min/$Kg^{0.75}$) [defined as [(4.545xVCO_2)-(3.205xVO_2)] /1000]; and Lipid Oxidation (g/min/$Kg^{0.75}$) [defined as [1.672x(VO_2-VCO_2)]/1000] were calculated from VO_2 and VCO_2 data. To remove variance in metabolic parameters derived from differences in body weight between animals, analysis of covariance (ANCOVA) was performed. ANCOVA is a robust method to compare groups with divergent body weights and composition[64,65]. For data obtained in mice on a normal diet, values of O_2 consumption and CO_2 production were referred to an adjusted mean body weight of 25.8071 g determined with ANCOVA, using body weight as a covariate in WT and RAP250 male mice in normal diet. In acute cold exposure studies, a Sable Systems Promethion Core was used. In these studies, mice were acclimated to the cages during 4 days at 22 °C and subjected to 4 °C during 8 hours. Mice were sacrificed and brown adipose tissues were collected.

Body composition analysis

Mouse body composition was measured using Quantitative Magnetic Resonance with the EchoMRI™ Body Composition Analyzer.

Measurement of glucose oxidation activity

Glucose oxidation was determined using radioactive glucose (D-[U]-^{14}C-glucose, Amersham Biosciences).

30-week-old male mice were killed by cervical dislocation; BAT was harvested and kept in cold Washing Buffer (KRBH solution, 1% (w/v) BSA (Albumin bovine serum, fraction V, minimum 96% lyophilized)), until further processing. BAT samples were then transferred to Digestion Buffer (KRBH solution, 3.5% (w/v) BSA, 0.5 mg/ml glucose (D(+)-glucose anhydrous), 1 mg/ml Collagenase type II from Clostridium histolyticum), at a ratio of 10 ml Digestion Buffer per gram of tissue. They were then mechanically minced and allowed to digest at 37 °C and under 250 rpm shaking for 30'–1 h. Undigested material was discarded by using a 100-µm strainer. The BAT digestion solution was diluted (to lower collagenase activity) and used directly. For glucose oxidation, 0.5 ml adipocyte solution was incubated for 4 h with 0.5 ml Oxidation Buffer (KRBH solution, 1% (w/v) BSA, 5 mmol/L glucose, 1 µCi/mL (D-[U]-^{14}C-glucose) in 6-well plates, and CO_2 was collected as in ref. 61. Data are expressed as nmol of glucose/h corrected by DNA content. Glucose oxidation from wild-type tissues was used as 100% value.

Electron microscopy

Approximately 1-mm^3 pieces of BAT were fixed in 2% paraformaldehyde and 2.5% glutaraldehyde in phosphate buffer. The protocol is described in ref. 66. Sections were observed under a JEM-1010 electron microscope (Jeol, Japan) equipped with a CCD camera SIS Megaview III and the AnalySIS software.

Histology

BAT, adipose tissue depots and liver were fixed in 10% formaldehyde in methanol and then paraffin-embedded. Sections were subjected to standard Hematoxylin/Eosin (HE) staining. Images were acquired with a NanoZoomer-2.0 HT C9600 digital scanner (Hamamatsu, Photonics, France) equipped with a 20X objective and coupled to a mercury lamp unit L11600-05 and using NDP.scan2.5 software U10074-03 (Hamamatsu, Photonics, France). Adipocyte area was measured using open software ImageJ (W. Rasband, National Institute of Mental Health, Bethesda, Maryland, USA). Liver fat content was estimated from HE-stained slides using the CTAn software (SkyScan, Kontich, Belgium). DAPI/Wheat Germ Agglutinin (WGA)/UCP1 staining was performed as reported[67].

Mouse RNA extraction and real-time PCR

RNA from various tissues was extracted using a protocol combining TRIZOL reagent (Invitrogen, Carlsbad, CA, USA) and RNAeasy® minikit columns (Qiagen. Alameda, CA, USA), following the manufacturer's instructions. RNA was reverse-transcribed with the SuperScript RTII kit (Invitrogen, Carlsbad Ca, USA). PCRs were performed using the ABI Prism 7900 HT real-time PCR machine (Applied Biosystems, USA) and the SYBR® Green PCR Master Mix (Applied Biosystems, USA), or Taqman Master Mix. The thermal protocol was 10 min at 95 °C, followed by 40 cycles of 15'/95 °C–60'/60 °C. All measurements for mouse mRNA were normalized to *Arp*. For each designed primer set, a melting curve of PCR products was performed to verify unspecific amplification or primer-dimer formation. The results were analyzed with the system SDS software. The primers used are specified in Table S2.

DNA extraction

Total DNA was extracted from mouse interscapular BAT, inguinal subcutaneous Adipose tissue (SAT) and perigonadal adipose tissue (PAT). Tissue was digested with proteinase K (Merck Life Science S.L.U., 03115801001) and total DNA was purified using DNeasy Blood & Tissue Kit (Qiagen, 69504). Total cellular DNA (1 ng DNA) is used as a template and is amplified with specific primers for *Cox2* gene, as a mitochondrial gene (*Cox2*f: CTACAAGACGCCACAT and *Cox2*r: GAGAGGGGAGAGCAAT) and for *Sdha* gene, as a nuclear gene (*Sdha*f: TACTACAGCCCCAAGTCT, *Sdha*r: TGGACCCATCTTCTATGC) by Real-Time PCR using SYBRGreen. The ratio genomic-nuclear DNA/ mtDNA was calculated.

RNA-seq

The concentration of total RNA in preparations was quantified with Nanodrop One (Thermo Fisher), and RNA integrity was assessed using the Bioanalyzer 2100 RNA Nano assay (Agilent). Libraries for RNA-seq were prepared at IRB Barcelona's Functional Genomics Core Facility. Briefly, mRNA was isolated from 1.2 µg of total RNA using the kit NEBNext Poly(A) mRNA Magnetic Isolation Module (New England Biolabs). NGS libraries for RNA-seq were prepared from the purified mRNA using the NEBNext Ultra II RNA Library Prep Kit for Illumina (New England Biolabs). Seven (WT/RAP250) and eight (Control/UCP1-NRN1) cycles of PCR amplification were applied to all libraries. Libraries were quantified using the Qubit dsDNA HS assay (Invitrogen) and quality controlled with the Bioanalyzer 2100 DNA HS assay (Agilent), for WT/RAP250 BAT, and Tapestation HS D5000 assay (Agilent) for Control/NRN1 BAT.

For WT/RAP250 BAT RNA-seq an equimolar pool was prepared with the nine libraries and subjected to sequencing at the Centre for Genomic Regulation. A final qPCR quality control was performed before sequencing in one lane of an Illumina HiSeq2500. Sequencing output was 270 million 50-bp single-end reads, and at least 28 million reads were obtained for all samples.

For Control/UCP1 BAT RNAseq an equimolar pool was prepared with the nine libraries and subjected to paired-end 150 nt sequencing on a NovaSeq6000 S4 (Illumina). More than 121 Gbp of reads were produced, with a minimum of 39 million of paired-end reads per sample.

FastQ files were aligned against the Mus musculus mm10 genome with STAR 2.5.2b[68] using default options. Aligned reads were used to obtain raw counts at mm10 NCBI RefSeq gene level using featureCounts from Rsubread version 1.32.4[69] with options minMQS=1. DESeq2 1.22.2[70] was used to find differentially expressed genes in KO vs WT. Genes were selected as differentially expressed with thresholds $|FC| > 1.5$ and Benjamini-Hochberg adjusted $P < 0.1$. For functional enrichment analysis (GSEA), regularized log transformation (rlog) was applied to read counts using DESeq2 and rotation gene set testing using the maxmean statistic was performed[71]. For cell type deconvolution analyses, the DWLS algorithm (https://github.com/dtsoucas/DWLS) was used with reference single cell data obtained from ref. 72. All analyses were performed in R-3.5.1 (R Core Team, 2018).

Isolation, immortalization and culture of brown preadipocytes

Immortalized brown preadipocytes were generated as described in refs. 67,73. Retroviral vector pBabe encoding SV40 LT-Puro antigen was purchased from Addgene. Cells were grown in monolayer culture in DMEM supplemented with 10% (v/v) fetal bovine serum (FBS) (v/v) antibiotics (10,000 units/ml penicillin G and 10 mg/ml streptomycin), and 25 mM Hepes (pH 7.4). The differentiation process is described in ref. 67.

Immortalized brown preadipocytes were also used to generate the NRN1 deficiency model. Lentivirus encoding for a shRNA scramble or against Nrn1 (TRCN0000177415 validated clone from Merk), as control (SCR) or knockdown (shNRN1), were produced in HEK 293 T cells (ATCC, CRL-11268) as reported[74]. Transduced cells were selected based on Puromycin resistance (Santa Cruz Biotechnology, sc-108071; 3 µg/ml).

Adipocytes and Stroma Vascular Fraction (SVF) extraction from brown adipose tissue

Adipocyes and SVF were obtained as reported[75,76].

NRN1 recombinant protein production

A DNA fragment encoding amino acids 28-115 inclusive of mouse Neuritin (Accession number NM_153529) was amplified using the following semi-nested primers:

NRN1fwdout gcgtagctgaaaccggccaccatcaccatcaccatgctagcgaaaac ctgtattttcagg

NRN1fwdin caccatgctagcgaaaacctgtattttcaggcgggcaagtgtgatgcag tctttaagggc

NRN1rev cggcctcgagcggccgcTTagttgctgctgccgcagagttcgaataagctg

and KOD polymerase. The resulting 343 bp fragment was purified using AMPure (Beckman Coulter) before InFusion (Takara Bio) into KpnI and NotI-cut pOPINTTG[77]. The resulting construct will produce the following protein when expressed in mammalian cells:

MGILPSPGMPALLSLVSLLSVLLMGCVA ↓ETGHHHHHHASENLYFQ↓ AGKCDAVFKGFSDCLLKLGDSMANYPQGLDDKTNIKTVCTYWEDFHSCTV TALTDCQEGAKDMWDKLRKESKNLNIQGSLFELCGSSN*. The protein consists of the μ-phosphatase signal peptide (with signal peptidase site indicated, first ↓, a Hexa-histidine tag and TEV cleavage site (indicated, second ↓) followed by amino acids 28-115 of mouse Neuritin. This protein will be secreted, can be purified by Immobilized Metal Affinity Chromatography (IMAC) and can then be cleaved with TEV protease to produce mature 'soluble' NRN1 (this construct is truncated to also exclude the GPI-anchored G116).

293-6E cells[78] were cultured in shaken flasks in F-17 Freestyle media (Gibco) supplemented with GlutaMax, Poloxamer 188 and G418 (final concentrations of 4 mM, 0.1% and 25 μg/ml, respectively) at 37 °C in 5% CO_2. At a density of approximately 2.0 × 106 cells/ml cells were transfected with a 1:4 polyplex of plasmid DNA:PEI MAXX at a concentration of 1 mg plasmid DNA/litre of cells. After 24 h the media was supplemented with sterile TN1 solution (Tryptone N1, TekniScience Inc. to 0.5% w/v in F-17 Freestyle media). After a further 96 hours the media was cleared by pelleting the cells by centrifugation at 500 × *g* then 5000 *g* followed filtration through Whatman 3 M paper filters. All further steps were performed at 4 °C.

Urea was added to a final concentration of 4 M and the pH adjusted to pH 7.5 before the sample was applied to a 5 ml Excel IMAC column equilibrated with IMAC Wash Buffer (Tris pH8 50 mM, NaCl 150 mM, Urea 4 M, Imidazole 20 mM, DTT 2 mM). His-NRN was eluted with IMAC Elution Buffer (Tris pH8 50 mM, NaCl 150 mM, Urea 4 M, Imidazole 500 mM, DTT 2 mM). His-NRN containing fractions were pooled and buffer exchanged to Digest Buffer (Tris pH8 50 mM, NaCl 500 mM, Urea 2 M, DTT 2 mM) using a HiPrep 26/10 Desalt column before the addition of His-tagged TEV protease at a 1:25 His-TEV:His-NRN ratio and incubation overnight at 4 °C.

The TEV-digested sample was first passed through a 1 ml Excel HisTrap column to capture uncut His-NRN and His-TEV before size exclusion chromatography (SEC) was performed on a Superdex 30 pg 16/600 column equilibrated with Tris pH8 20 mM, NaCl 150 mM, Urea 6 M, DTT 2 mM, EDTA 2 mM.

Peak fractions were buffer exchanged (as before, using a HiPrep 26/10 Desalt column) into phosphate-buffered saline (PBS) before use.

Cell treatments

Adipocytes (Scr and shNRN1) at day 10 of differentiation were stimulated with Isoproterenol (10 uM) in DMEM with 10% FBS for 2 h. Cells were lysed to obtain RNA or total cell extracts. Media was kept and centrifuged at 4 °C at 1000 × *g* for 20 min to remove any precipitate and then stored at −20 °C.

For the detection of proteins phosphorylated by PKA (p-PKA substrates) control adipocytes were washed in PBS twice and were incubated during two hours in media without serum. Cells were treated with NRN1 at different concentration during 2 h and then total cell extracts were obtained.

For NRN1 chronic studies, brown adipocytes at day 4 of differentiation were treated with NRN1 at 100 ng/ml in the presence of differentiation medium. NRN1 was maintained during all the process of differentiation.

Cell extracts, tissue extracts, and western blot

Cells were washed twice in cold phosphate-buffered saline (PBS) and lysed in Triton X-100 lysis buffer (50 mM Tris−HCl pH 7.5, 100 mM NaCl, 50 mM NaF, 5 mM EDTA, 40 mM β-glycerophosphate, 1% Triton X-100 and protease inhibitor cocktail (ROCHE)) for 15 min at 4 °C. Insoluble material was removed by centrifugation at 12,000 × *g* for 5 min at 4 °C.

Tissue samples were homogenized in 10 vol of lysis buffer [50 mM Tris (pH 7.5), 150 mM NaCl, 1% Triton X-100, 2 mM EDTA, 2 mM sodium orthovanadate, 50 mM NaF, 20 mM sodium pyrophosphate, and protease inhibitor cocktail (Roche)] with a disperser homogenizer (Ika Ultra-Turrax® T25basic, S25N-10G probe). Homogenates were rotated for 1 h at 4 °C in an orbital shaker and centrifuged at 16,000 x *g* for 15 min at 4 °C. Proteins from total homogenates were resolved in 8% (RAP250 detection) or 10% acrylamide gels for SDS/PAGE and transferred to Immobilon membranes (Millipore). Proteins were detected by the ECL method and quantified by densitometry using Genetools from Syngene or by NIR-fluorescence detected with LI-COR Odyssey System and measured with Image Studio software.

The following antibodies were used: RAP250 (ASC2 antibody BL1874, Bethyl laboratories and NCOA6 polyclonal antibody 25241-1_AP, Proteintech); p-HSL (S563, #4139), HSL (#4107), P-PKA substrates (#9624), βactin (AC-15, SIGMA); α-tubulin (SIGMA); Vinculin (Abcam); GAPDH (2118S, Cell Signaling), UCP1 (ab10983 Abcam); PPARγ and C/EBPα (Santa Cruz); total OXPHOS rodent WB antibody cocktail (ab110413, Abcam), ADRB3 (bs-1063R Bioss Antibodies), NRN1 (B-9 Santa Cruz and AF283 from Biotechne R&D Systems); TH (R&D Systems MAB7566SP and ab6211 from Abcam).

Seahorse mitochondrial respiration studies

Preadipocytes (Scr/ ShNRN1) were plated, grown and differentiated as it is described in ref. 67 For NRN1 treated cells, recombinant NRN1 protein was added chronically at day 4 of differentiation until d9-d10 at a final concentration of 100 ng/ml. Media was changed every two days. Seahorse experiments were performed as reported[79].

NRN1 Elisa in plasma and cell medium

Neuritin 1 (NRN1) ELISA Kit (Catalog No: abx155876, Abbexa) was used to measure Nrn1 from mouse plasma and cell culture media. 75 μl of plasma and 300 μl of culture media were used following a commercial protocol.

Statistical analysis

Data are presented as mean ± SEM. Statistical significance was determined by two-tailed t-Student test, or by two-way ANOVA (Šidak's multiple comparisons test or by an Ordinary two-way ANOVA), or by Covariance (ANCOVA) with weight as the covariate. Significance was established at $P < 0.05$.

Reporting summary

Further information on research design is available in the Nature Portfolio Reporting Summary linked to this article.

Data availability

All data generated or analyzed during this study are included in this published article (and its supplementary information and Source Data files). The complete transcriptomic datasets were deposited to the National Center for Biotechnology Information's Gene Expression Omnibus Database and are accessible through GEO Series accession number GSE295442 and GSE295443. Source data are provided with this paper. All data supporting the findings is also available from the corresponding author upon request. Source data are provided with this paper.

References

1. Apovian, C. M. The clinical and economic consequences of obesity. *Am. J. managed care* **19**, s219–228 (2013).
2. Simonnet, A. et al. High Prevalence of Obesity in Severe Acute Respiratory Syndrome Coronavirus-2 (SARS-CoV-2) Requiring Invasive Mechanical Ventilation. *Obesity* **28**, 1195–1199 (2020).
3. Ayres, J. S. A metabolic handbook for the COVID-19 pandemic. *Nat. Metab.* **2**, 572–585 (2020).
4. Cypess, A. M. et al. Identification and importance of brown adipose tissue in adult humans. *N. Engl. J. Med.* **360**, 1509–1517 (2009).
5. Nedergaard, J., Bengtsson, T. & Cannon, B. Unexpected evidence for active brown adipose tissue in adult humans. *Am. J. Physiol. Endocrinol. Metab.* **293**, E444–452 (2007).
6. Saito, M. et al. High incidence of metabolically active brown adipose tissue in healthy adult humans: effects of cold exposure and adiposity. *Diabetes* **58**, 1526–1531 (2009).
7. Nedergaard, J. & Cannon, B. The changed metabolic world with human brown adipose tissue: therapeutic visions. *Cell Metab.* **11**, 268–272 (2010).
8. Cannon, B. & Nedergaard, J. Brown adipose tissue: function and physiological significance. *Physiological Rev.* **84**, 277–359 (2004).
9. Pinckard, K. M. & Stanford, K. I. The heartwarming effect of brown adipose tissue. *Mol. Pharmacol.* **102**, 460–471 (2022).
10. Cereijo, R. et al. CXCL14, a brown adipokine that mediates brown-fat-to-macrophage communication in thermogenic adaptation. *Cell Metab.* **28**, 750–763.e756 (2018).
11. Keipert, S. et al. Genetic disruption of uncoupling protein 1 in mice renders brown adipose tissue a significant source of FGF21 secretion. *Mol. Metab.* **4**, 537–542 (2015).
12. Hui, X. et al. Adiponectin enhances cold-induced browning of subcutaneous adipose tissue via promoting m2 macrophage proliferation. *Cell Metab.* **22**, 279–290 (2015).
13. Kong, X. et al. Brown adipose tissue controls skeletal muscle function via the secretion of myostatin. *Cell Metab.* **28**, 631–643.e633 (2018).
14. Deshmukh, A. S. et al. Proteomics-based comparative mapping of the secretomes of human brown and white adipocytes reveals epdr1 as a novel batokine. *Cell Metab.* **30**, 963–975.e967 (2019).
15. Wang, G. X. et al. The brown fat-enriched secreted factor Nrg4 preserves metabolic homeostasis through attenuation of hepatic lipogenesis. *Nat. Med.* **20**, 1436–1443 (2014).
16. Whittle, A. J. et al. BMP8B increases brown adipose tissue thermogenesis through both central and peripheral actions. *Cell* **149**, 871–885 (2012).
17. Zeng, X. et al. Innervation of thermogenic adipose tissue via a calsyntenin 3beta-S100b axis. *Nature* **569**, 229–235 (2019).
18. Tseng, Y. H. et al. New role of bone morphogenetic protein 7 in brown adipogenesis and energy expenditure. *Nature* **454**, 1000–1004 (2008).
19. Mahajan, M. A. & Samuels, H. H. Nuclear hormone receptor coregulator: role in hormone action, metabolism, growth, and development. *Endocr. Rev.* **26**, 583–597 (2005).
20. Goo, Y. H. et al. Activating signal cointegrator 2 belongs to a novel steady-state complex that contains a subset of trithorax group proteins. *Mol. Cell. Biol.* **23**, 140–149 (2003).
21. Lee, S. et al. Coactivator as a target gene specificity determinant for histone H3 lysine 4 methyltransferases. *Proc. Natl Acad. Sci. USA* **103**, 15392–15397 (2006).
22. Mahajan, M. A. & Samuels, H. H. Nuclear receptor coactivator/coregulator NCoA6(NRC) is a pleiotropic coregulator involved in transcription, cell survival, growth and development. *Nucl. receptor Signal.* **6**, e002 (2008).
23. Li, Q., Chu, M. J. & Xu, J. Tissue- and nuclear receptor-specific function of the C-terminal LXXLL motif of coactivator NCoA6/AIB3 in mice. *Mol. Cell. Biol.* **27**, 8073–8086 (2007).
24. Kim, G. H. et al. Regulation of hepatic insulin sensitivity by activating signal co-integrator-2. *Biochemical J.* **447**, 437–447 (2012).
25. Burghardt, H. et al. The nuclear receptor coactivator AIB3 is a modulator of HOMA beta-cell function in nondiabetic children. *Clin. Endocrinol.* **69**, 730–736 (2008).
26. Yeom, S. Y. et al. Regulation of insulin secretion and beta-cell mass by activating signal cointegrator 2. *Mol. Cell. Biol.* **26**, 4553–4563 (2006).
27. Qi, C. et al. Transcriptional coactivator PRIP, the peroxisome proliferator-activated receptor gamma (PPARgamma)-interacting protein, is required for PPARgamma-mediated adipogenesis. *J. Biol. Chem.* **278**, 25281–25284 (2003).
28. Lee, J. et al. Targeted inactivation of MLL3 histone H3-Lys-4 methyltransferase activity in the mouse reveals vital roles for MLL3 in adipogenesis. *Proc. Natl Acad. Sci. USA* **105**, 19229–19234 (2008).
29. Marron, T. U. et al. Androgen-induced neurite outgrowth is mediated by neuritin in motor neurones. *J. Neurochemistry* **92**, 10–20 (2005).
30. Nedivi, E., Hevroni, D., Naot, D., Israeli, D. & Citri, Y. Numerous candidate plasticity-related genes revealed by differential cDNA cloning. *Nature* **363**, 718–722 (1993).
31. Nedivi, E., Fieldust, S., Theill, L. E. & Hevron, D. A set of genes expressed in response to light in the adult cerebral cortex and regulated during development. *Proc. Natl Acad. Sci. USA* **93**, 2048–2053 (1996).
32. Gao, R. et al. Exogenous Neuritin Promotes Nerve Regeneration After Acute Spinal Cord Injury in Rats. *Hum. gene Ther.* **27**, 544–554 (2016).
33. Mahajan, M. A., Das, S., Zhu, H., Tomic-Canic, M. & Samuels, H. H. The nuclear hormone receptor coactivator NRC is a pleiotropic modulator affecting growth, development, apoptosis, reproduction, and wound repair. *Mol. Cell. Biol.* **24**, 4994–5004 (2004).
34. Rothwell, N. J., Stock, M. J. & Warwick, B. P. The effect of high fat and high carbohydrate cafeteria diets on diet-induced thermogenesis in the rat. *Int. J. Obes.* **7**, 263–270 (1983).
35. Mercer, S. W. & Trayhurn, P. Effect of high fat diets on the thermogenic activity of brown adipose tissue in cold-acclimated mice. *J. Nutr.* **114**, 1151–1158 (1984).
36. Lorsignol, A., Rabiller, L., Labit, E., Casteilla, L. & Penicaud, L. The nervous system and adipose tissues: a tale of dialogues. *Am. J. Physiol. Endocrinol. Metab.* **325**, E480–E490 (2023).
37. Blaszkiewicz, M., Willows, J. W., Johnson, C. P. & Townsend, K. L. The importance of peripheral nerves in adipose tissue for the regulation of energy balance. *Biology* **8** (2019)
38. Angueira, A. R. et al. Early B Cell Factor Activity Controls Developmental and Adaptive Thermogenic Gene Programming in Adipocytes. *Cell Rep.* **30**, 2869–2878 (2020).
39. Cypess, A. M. et al. Activation of human brown adipose tissue by a beta3-adrenergic receptor agonist. *Cell Metab.* **21**, 33–38 (2015).
40. Costanzo, M. C. et al. The Type 2 Diabetes Knowledge Portal: An open access genetic resource dedicated to type 2 diabetes and related traits. *Cell Metab.* **35**, 695–710 (2023).
41. Kuang, S. Q. et al. Deletion of the cancer-amplified coactivator AIB3 results in defective placentation and embryonic lethality. *J. Biol. Chem.* **277**, 45356–45360 (2002).
42. Antonson, P. et al. Inactivation of the nuclear receptor coactivator RAP250 in mice results in placental vascular dysfunction. *Mol. Cell. Biol.* **23**, 1260–1268 (2003).
43. Oh, G. S. et al. Regulation of Hepatic Gluconeogenesis by Nuclear Receptor Coactivator 6. *Molecules cells* **45**, 180–192 (2022).

44. Himms-Hagen, J., Hogan, S. & Zaror-Behrens, G. Increased brown adipose tissue thermogenesis in obese (ob/ob) mice fed a palatable diet. *Am. J. Physiol.* **250**, E274–281 (1986).
45. Naeve, G. S. et al. Neuritin: a gene induced by neural activity and neurotrophins that promotes neuritogenesis. *Proc. Natl Acad. Sci. USA* **94**, 2648–2653 (1997).
46. Zito, A. et al. Neuritin 1 promotes neuronal migration. *Brain Struct. Funct.* **219**, 105–118 (2014).
47. Fujino, T. et al. CPG15 regulates synapse stability in the developing and adult brain. *Genes Dev.* **25**, 2674–2685 (2011).
48. Zhao, Q. R. et al. Neuritin reverses deficits in murine novel object associative recognition memory caused by exposure to extremely low-frequency (50 Hz) electromagnetic fields. *Sci. Rep.* **5**, 11768 (2015).
49. Gonzalez-Figueroa, P. et al. Follicular regulatory T cells produce neuritin to regulate B cells. *Cell* **184**, 1775–1789.e1719 (2021).
50. Fagerberg, L. et al. Analysis of the human tissue-specific expression by genome-wide integration of transcriptomics and antibody-based proteomics. *Mol. Cell. Proteom.: MCP* **13**, 397–406 (2014).
51. Piunti, A. & Shilatifard, A. Epigenetic balance of gene expression by Polycomb and COMPASS families. *Science* **352**, aad9780 (2016).
52. Hu, D. et al. The MLL3/MLL4 branches of the COMPASS family function as major histone H3K4 monomethylases at enhancers. *Mol. Cell. Biol.* **33**, 4745–4754 (2013).
53. Lee, M. G. et al. Demethylation of H3K27 regulates polycomb recruitment and H2A ubiquitination. *Science* **318**, 447–450 (2007).
54. Pellegrinelli, V. et al. Adipocyte-secreted BMP8b mediates adrenergic-induced remodeling of the neuro-vascular network in adipose tissue. *Nat. Commun.* **9**, 4974 (2018).
55. Yu, H. et al. Neurotrophic factor Neuritin modulates T cell electrical and metabolic state for the balance of tolerance and immunity. *eLife* **13** (2024).
56. Bosserhoff, A. K., Schneider, N., Ellmann, L., Heinzerling, L. & Kuphal, S. The neurotrophin Neuritin1 (cpg15) is involved in melanoma migration, attachment independent growth, and vascular mimicry. *Oncotarget* **8**, 1117–1131 (2017).
57. Yao, J. J. et al. Neuritin activates insulin receptor pathway to up-regulate Kv4.2-mediated transient outward K+ current in rat cerebellar granule neurons. *J. Biol. Chem.* **287**, 41534–41545 (2012).
58. Shimada, T., Yoshida, T. & Yamagata, K. Neuritin Mediates Activity-Dependent Axonal Branch Formation in Part via FGF Signaling. *J. Neurosci.: Off. J. Soc. Neurosci.* **36**, 4534–4548 (2016).
59. Yao, J. J., Zhao, Q. R., Lu, J. M. & Mei, Y. A. Functions and the related signaling pathways of the neurotrophic factor neuritin. *Acta pharmacologica Sin.* **39**, 1414–1420 (2018).
60. Jimenez, V. et al. In vivo adeno-associated viral vector-mediated genetic engineering of white and brown adipose tissue in adult mice. *Diabetes* **62**, 4012–4022 (2013).
61. Sebastian, D. et al. Mitofusin 2 (Mfn2) links mitochondrial and endoplasmic reticulum function with insulin signaling and is essential for normal glucose homeostasis. *Proc. Natl Acad. Sci. USA* **109**, 5523–5528 (2012).
62. Perrin, C., Knauf, C. & Burcelin, R. Intracerebroventricular infusion of glucose, insulin, and the adenosine monophosphate-activated kinase activator, 5-aminoimidazole-4-carboxamide-1-beta-D-ribofuranoside, controls muscle glycogen synthesis. *Endocrinology* **145**, 4025–4033 (2004).
63. Judex, S. et al. Quantification of adiposity in small rodents using micro-CT. *Methods* **50**, 14–19 (2010).
64. Arch, J. R., Hislop, D., Wang, S. J. & Speakman, J. R. Some mathematical and technical issues in the measurement and interpretation of open-circuit indirect calorimetry in small animals. *Int J. Obes. (Lond.)* **30**, 1322–1331 (2006).
65. Tschop, M. H. et al. A guide to analysis of mouse energy metabolism. *Nat. methods* **9**, 57–63 (2011).
66. Soro-Arnaiz, I. et al. Role of Mitochondrial Complex IV in Age-Dependent Obesity. *Cell Rep.* **16**, 2991–3002 (2016).
67. Sabate-Perez, A. et al. Autophagy-mediated NCOR1 degradation is required for brown fat maturation and thermogenesis. *Autophagy* **19**, 904–925 (2023).
68. Dobin, A. & Gingeras, T. R. Mapping RNA-seq Reads with STAR. *Curr. Protoc. Bioinforma.* **51**, 11 14 11–11 14 19 (2015).
69. Liao, Y., Smyth, G. K. & Shi, W. featureCounts: an efficient general purpose program for assigning sequence reads to genomic features. *Bioinformatics* **30**, 923–930 (2014).
70. Love, M. I., Huber, W. & Anders, S. Moderated estimation of fold change and dispersion for RNA-seq data with DESeq2. *Genome Biol.* **15**, 550 (2014).
71. Caballe-Mestres, A., Berenguer-Llergo, A. & Stephan-Otto Attolini, C. Roastgsa: a comparison of rotation-based scores for gene set enrichment analysis. *BMC Bioinforma.* **24**, 408 (2023).
72. Shamsi, F. et al. Vascular smooth muscle-derived Trpv1(+) progenitors are a source of cold-induced thermogenic adipocytes. *Nat. Metab.* **3**, 485–495 (2021).
73. Klein, J. et al. β3-Adrenergic Stimulation Differentially Inhibits Insulin Signaling and Decreases Insulin-induced Glucose Uptake in Brown Adipocytes. *J. Biol. Chem.* **274**, 34795–34802 (1999).
74. Baumgartner, B. G. et al. Identification of a novel modulator of thyroid hormone receptor-mediated action. *PloS one* **2**, e1183 (2007).
75. Castillo, A. et al. Adipocyte MTERF4 regulates non-shivering adaptive thermogenesis and sympathetic-dependent glucose homeostasis. *Biochimica et. biophysica acta Mol. basis Dis.* **1865**, 1298–1312 (2019).
76. Enguix, N. et al. Mice lacking PGC-1beta in adipose tissues reveal a dissociation between mitochondrial dysfunction and insulin resistance. *Mol. Metab.* **2**, 215–226 (2013).
77. Berrow, N. S. et al. A versatile ligation-independent cloning method suitable for high-throughput expression screening applications. *Nucleic acids Res.* **35**, e45 (2007).
78. Durocher, Y., Perret, S. & Kamen, A. High-level and high-throughput recombinant protein production by transient transfection of suspension-growing human 293-EBNA1 cells. *Nucleic acids Res.* **30**, E9 (2002).
79. Oeckl, J., Bast-Habersbrunner, A., Fromme, T., Klingenspor, M. & Li, Y. Isolation, culture, and functional analysis of murine thermogenic adipocytes. *STAR Protoc.* **1**, 100118 (2020).

Acknowledgements

We thank J. Seco for technical assistance. We also thank the Functional Genomics, Biostatistics/Bioinformatics and Histopathology Facilities at IRB Barcelona, and the Cytometry and Electron Microscopy at the CCiT-UB. S.R.V. was a predoctoral fellow of the Fundaçao para a Ciência e Tecnologia - Ministério da Ciência, Tecnologia e Ensino Superior, Portugal. This study was supported by research grants from MICINN (PID2022-137576OB-I00), Generalitat de Catalunya, INFLAMES (PIE-14/00045) Instituto de Salud Carlos III, CIBERDEM ("Instituto de Salud Carlos III"), CIBEREHD and Fondo de Investigaciones Sanitarias (PI22/00526); Junta de Castilla y Leon" (SA113/P23); Fundación Ramon Areces (CIVP18A3942), Fundación BBVA, the Fundació Marató de TV3 (20132330 and 201916-31), the European Foundation for the Study of Diabetes (EFSD) and AFM Téléthon. A.Z. is a recipient of an ICREA "Academia" Award (Generalitat de Catalunya). We gratefully acknowledge institutional funding from MINECO through the Centres of Excellence Severo Ochoa Award, and from the CERCA Programme of the Generalitat de Catalunya. JAG is thankful for support from the Robert A. Welch Foundation (E-0004) and the Swedish Science Council.

Author contributions

Funding acquisition: A.Z., and J.A.G.; conceptualization: M.S.F. and A.Z.; investigation and formal analysis: M.o.R., S.R.V., N.B.F., N.B., Ma.R., N.G., A.R.F., A.S.B., A.R.P., L.R.C., H.B., D.S., N.P., V.H., L.I.A., O.R., M.J.M., J.J.G.M., R.B., and P.A.; visualization, M.S.F., M.P. and A.Z.; writing, M.S.F. and A.Z.; writing review & edit, M.S.F. and A.Z.; Supervision, M.S.F. and A.Z.

Competing interests

The authors declare no competing interests.

Additional information

Supplementary information The online version contains supplementary material available at https://doi.org/10.1038/s41467-025-62255-2.

Correspondence and requests for materials should be addressed to Manuela Sánchez-Feutrie or Antonio Zorzano.

Peer review information *Nature Communications* thanks the anonymous reviewer(s) for their contribution to the peer review of this work. A peer review file is available.

Reprints and permissions information is available at http://www.nature.com/reprints

Publisher's note Springer Nature remains neutral with regard to jurisdictional claims in published maps and institutional affiliations.

[1]Institute for Research in Biomedicine (IRB Barcelona), The Barcelona Institute of Science and Technology, Baldiri Reixac 10, 08028 Barcelona, Spain. [2]Departament de Bioquímica i Biomedicina Molecular, Facultat de Biologia, Universitat de Barcelona, Av. Diagonal 645, 08028 Barcelona, Spain. [3]Departament de Biologia Cel.lular, Fisiologia i Immunologia, Facultat de Biologia, Universitat de Barcelona, Av. Diagonal 645, 08028 Barcelona, Spain. [4]CIBER de Diabetes y Enfermedades Metabólicas Asociadas (CIBERDEM), Instituto de Salud Carlos III, Madrid, Spain. [5]Institut de Biomedicina de la Universitat de Barcelona (IBUB), Universitat de Barcelona (UB), 08028 Barcelona, Spain. [6]Experimental Hepatology and Drug Targeting (HEVEPHARM), Universidad de Salamanca; Instituto de Investigación Biomédica de Salamanca (IBSAL), Centro de Investigación Biomédica en Red de Enfermedades Hepáticas y Digestivas (CIBEREHD), ISCIII, Madrid, Spain. [7]CIBER de Enfermedades Raras (CIBERER), Instituto de Salud Carlos III, Madrid, Spain. [8]UMR 1297 INSERM, Team INCOMM Rangueil Hospital, Toulouse 31400, France. [9]Department of Medicine Huddinge, Karolinska Institutet, Neo, SE-141 83, Huddinge, Sweden. [10]Center for Nuclear Receptors and Cell Signaling, Department of Biology and Biochemistry, University of Houston, Houston, TX 77204, USA. [11]Present address: Medical BioSciences department, RadboudUMC, Geert Grooteplein 28, 6525 GA Nijmegen, The Netherlands. [12]Present address: Department of Internal Medicine, Erasmus MC, University Medical Center Rotterdam, Rotterdam, The Netherlands. [13]Present address: Unit of Molecular Metabolism, Lund University Diabetes Centre, SE-20213 Malmö, Sweden. [14]Present address: Novo Nordisk Foundation Center for Basic Metabolic Research, Faculty of Health and Medical Sciences, University of Copenhagen, Copenhagen 2200, Denmark. [15]Present address: Department of Biochemistry and Physiology, School of Pharmacy and Food Sciences, University of Barcelona, 08028 Barcelona, Spain. ✉e-mail: manuela.sanchez@irbbarcelona.org; antonio.zorzano@irbbarcelona.org